



**university of  
 groningen**

**faculty of mathematics  
 and natural sciences**

**POLYMER – NANOCRYSTAL TANDEM SOLAR CELLS  
 FOR ENHANCED POWER CONVERSION  
 EFFICIENCIES**

Bart Groeneveld

Supervisors:

Prof. Dr. M.A. Loi

M.J. Speirs, MSc

*This Master's thesis is submitted by:*

Bart Groeneveld

Student number: 1914022

*To the:*

Faculty of Mathematics and Natural Sciences

University of Groningen

*As required for completion of the degree:*

MSc Applied Physics

*The research was done in the group:*

Photophysics and OptoElectronics

*Supervisors:*

Prof. dr. Maria Antonietta Loi

Mark Speirs, MSc

June 2015

# Contents

Abstract .....	1
Acknowledgements .....	2
Chapter 1 Introduction.....	3
Chapter 2 Theory.....	5
2.1 Lead sulfide nanocrystals .....	5
2.2 Organic semiconductors.....	6
2.3 General solar cell .....	7
2.4 Non-ideal solar cell.....	12
2.5 PbS nanocrystal solar cells.....	13
2.6 Organic solar cells .....	15
2.7 Tandem solar cells .....	17
Chapter 3 Materials .....	21
3.1 P3HT .....	21
3.2 PCPDTBT.....	21
3.3 P3TI.....	22
3.4 PC <sub>60</sub> BM.....	22
3.5 PC <sub>70</sub> BM.....	22
3.6 PbS nanocrystals.....	22
3.7 Interlayer .....	23
3.8 ITO .....	24
3.9 PEDOT:PSS .....	24
3.10 Cathode .....	24
Chapter 4 Experimental.....	25
4.1 Cleaning substrates .....	25
4.2 Preparing solutions .....	25
4.3 Spincoating.....	26
4.4 Thermal evaporation .....	27
4.5 Total procedure for device fabrication.....	27
4.6 J-V measurements .....	28

4.7 EQE measurements .....	28
4.8 Absorbance .....	29
4.9 Thickness measurements .....	30
4.10 Light intensity measurements.....	30
4.11 Optical simulations .....	30
Chapter 5 Results.....	32
5.1 P3HT:PCBM – PbS tandem .....	32
5.2 PCPDTBT:PCBM – PbS tandem.....	36
5.3 P3TI:PC <sub>70</sub> BM – PbS tandem.....	40
5.4 P3TI:PC <sub>70</sub> BM – PbS tandem with LZO interlayer .....	43
5.5 P3HT:PCBM – PbS tandem with ZnO interlayer .....	46
Chapter 6 Conclusions.....	56
Bibliography .....	58

## Abstract

The work described in this thesis was carried out for the Master Applied Physics at the University of Groningen. The thesis focuses on a novel type of solar cell: a series-connected tandem solar cell consisting of a polymer-fullerene blend subcell in combination with a subcell made of lead sulfide nanocrystals. These two classes of materials have been used extensively in photovoltaic research on single solar cells. The main advantages of using these solar cells are the low costs and ease of processing of the devices. However, the major challenge is that the efficiencies of these so-called thin film solar cells are relatively low, preventing them from competing with commercial silicon cells. The tandem structure makes it possible to use both materials in one device, which increases the maximum attainable efficiency greatly. In theory it is possible to exceed the efficiency of silicon cells with a tandem cell. It is necessary to optimize all the layers in the tandem structure before this can become reality. In practice, this means that the thicknesses of the layers need to be fine-tuned for optimal charge generation in the device. In addition to this, the energy levels of all materials have to be aligned in such a way that the generated charges can be extracted efficiently. A very important role is that of the interlayer, which has to act as a recombination site to prevent the build-up of charges in the device. However, the interlayer has to meet more requirements and proved to be a delicate element in the design and fabrication of tandem solar cells. The experiments on the optimization of several polymer-fullerene - lead sulfide tandem structures are described in this work. These led to the fabrication of a P3HT:PCBM - PbS tandem cell with 1.64% power conversion efficiency. This efficiency was higher than that of the polymer subcell, and identical to the PCE of the lead sulfide subcell, suggesting that the tandem structure is capable of enhancing the efficiency of single solar cells.

## **Acknowledgements**

I am very grateful to prof. dr. Maria A. Loi for granting me the opportunity to carry out my master research in her group, and for her supervision and useful advice during my research. I also appreciate her help in finding an interesting internship.

I would also like to thank my supervisor Mark Speirs for his guidance and help during my project. Thank you for always being available to help me out with my questions or problems.

Finally, I want to thank all the people from the Photophysics and OptoElectronics group for their contribution to creating a good and enjoyable atmosphere to work in. My time in the group was great thanks to all of you!

## Chapter 1 Introduction

Due to the ever-increasing need for energy, the world is running out of fossil fuels. Renewable energy sources should be developed in order to sustain our energy consumption. Among all the alternative energy sources, photovoltaic energy is the most promising option to generate energy on such a scale that it can replace the fossil fuels. The efficiencies of commercial silicon solar cells lie around 23% [1], however, the price of these cells is very high which makes them less attractive for consumers. Cheaper alternatives for the expensive silicon cells are thin film solar cells. The thin film cells use less material than their silicon counterparts, which reduces their price. Moreover, they are cheaper to produce than silicon cells. This is due to the fact that the thin film devices are solution-processable, that is, they are made from a solution via techniques as spincoating or doctor blading. As a consequence, they can be made at a fraction of the cost of the silicon cells. Examples of materials that can be used in these thin film photovoltaic devices are lead sulfide (PbS) nanocrystals and polymers.

Nanocrystals are crystals with sizes on the order of nanometers. This size regime leads to interesting properties such as the discretization of the energy levels of the material. The size of the nanocrystals determines the extent of the splitting of the energy levels and therefore influences the band gap of the material. This property makes the nanocrystals very interesting for photovoltaic applications. The lead sulfide nanocrystals can be modified so that their absorption extends from the ultraviolet up to wavelengths in the near-infrared. This means that a large part of the solar spectrum can be absorbed by a PbS nanocrystal (NC) solar cell. As a result, solar cells with efficiencies as high as 8.5% have been reported [2, 3]. However, the absorption in the visible spectrum (400 – 700 nm) and the near-infrared (700 – 1400 nm) is low compared to the ultraviolet. Increased absorption in this range would enhance the efficiency of the device substantially.

Polymers are known to absorb mainly in the visible range of light. Their absorption is based on the conjugated bonds in the polymer, i.e., alternating single and double bonds along the carbon main chain of the material. They are used in thin film solar cells in combination with fullerenes for efficient photovoltaic performance. The efficiencies of polymer-fullerene, or organic, solar cells can be as high as 9% [4]. This means that both the lead sulfide nanocrystals and the polymer solar cells have lower efficiencies than the commercial silicon cells. In order to increase these efficiencies, a tandem structure can be used. This is a structure which consists of two solar cells (called subcells) electrically connected through an interlayer. The advantage of the tandem cell is that one can combine two materials with different absorption spectra, leading to an increased overall absorption of the solar spectrum. Research on organic tandem solar cells has led to efficiencies of 10.6% [5]. However, the materials used in this tandem absorb up to 900 nm and do therefore not absorb a lot of light in the near-infrared. When a material with a low band gap is used instead of one of the polymers, it is possible to increase the absorption for the tandem, resulting in a higher efficiency. The lead sulfide nanocrystals are an ideal candidate for the tandem cell due to the low band gap.

Recently, the first hybrid tandem solar cells consisting of an inorganic PbS layer and an organic P3HT:PCBM layer with an efficiency of 1.8% was made by our group [6]. This tandem device shows broad absorption up until 1100 nm, which is in the near-infrared. The absorption in the visible region between 450 and 600 nm is also increased with respect to both subcells. Increasing the efficiency of the device is possible by optimization of the device structure. For example, the thicknesses of the various layers can be adjusted to maximize the generated current. However, the biggest increase in device performance can be achieved when the structure of the device is altered.

The structure of the tandem cell is designed such that the low band gap PbS is in front of the higher band gap polymer-fullerene blend, i.e., the incident light first goes through the nanocrystal layer before it reaches the organic subcell. The lower band gap of the PbS NCs allows this material to absorb a large part of the incident light, resulting in a lower light intensity for the polymer-fullerene layer. When the order of the subcells is reversed, the higher band gap P3HT:PCBM blend is located in the front of the device. Incident light with an energy higher than the band gap of the polymer-fullerene blend can be absorbed; the light with lower energy passes through to the lead sulfide where it is absorbed. As a result, this tandem structure can generate more photocurrent and this can lead to higher efficiencies. This thesis describes the experiments that were carried out in order to fabricate tandem solar cells with a polymer front subcell and a lead sulfide nanocrystal back subcell. The next chapter will explain the theory behind the nanocrystals and polymers, as well as the use of these materials in solar cells.

## Chapter 2 Theory

### 2.1 Lead sulfide nanocrystals

Nanocrystals are crystalline materials consisting of hundreds or a few thousands atoms, therefore having dimensions between 2 to about 20 nm [7]. This means that the size regime of the nanocrystals lies somewhere between that of molecules and of bulk materials. This size regime leads to unique properties (e.g. electronic or optical) and these are dependent on the material of the NCs. The nanocrystals can, for example, be made of metals or semiconductors. An example of the application of metallic nanocrystals is the use of gold nanorods for molecular imaging in biological studies [8]. Semiconducting NCs are used in a number of optoelectronic devices, including light emitting diodes (LEDs), photodiodes and solar cells [9]. In this thesis, only the semiconducting nanocrystals will be covered, in particular the lead sulfide (PbS) NCs.

One of the most interesting properties of the nanocrystals is that the band gap of the material is tunable. The band gap of bulk PbS is 0.41 eV, which can be increased up to values greater than 1 eV [10]. The tuning of the band gap can be done by changing the size of the nanocrystal, where decreasing the size of the NC results in a higher band gap [11]. This is due to the quantum-size effect, in which the excitons (electron-hole pairs bound by the Coulomb interaction) in the material are confined in three dimensions. For this quantum-size effect to appear, the crystal size has to be smaller than the Bohr radius of the exciton. This results in discrete energy levels of the nanocrystal (so-called quantum-size levels) instead of the continuous energy bands of the bulk material [12]. A schematic representation of the quantum-size effect is shown in Figure 2.1. Band gap tuning gives the freedom to tune the absorption of the PbS through the size of the nanocrystals. This is very useful for photovoltaic applications where the absorption range of the materials is an important parameter. The size of the nanocrystals is determined during the synthesis of the material.

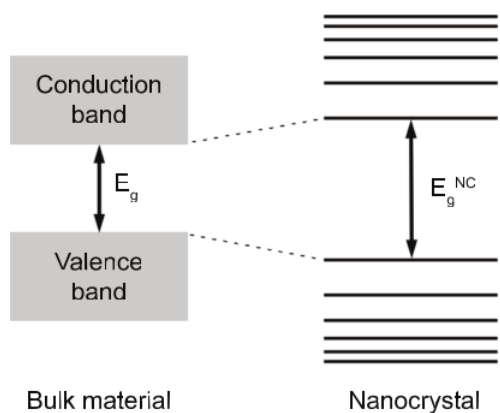


Figure 2.1: The quantum size effect results in a change in the band structure of the semiconducting material. The valence and conduction bands in the bulk material split up into discrete energy levels in the nanocrystal regime. In this regime the band gap is dependent on the size of the nanocrystal. [13]

The PbS NCs that have been used in this work are all colloidal solutions in chloroform. These nanocrystals have ligands (a functional molecular group) attached to them in order to prevent aggregation of the PbS nanocrystals. For the colloidal solutions, the ligands are oleic acid ( $C_{18}H_{34}O_2$ ) (see Figure 2.2a). Besides preventing the aggregation of PbS, the oleic acid also provides stability for the colloidal solution and its hydrophobic properties help the dissolution in non-polar solvents such as chloroform and toluene. However, the use of oleic acid has some major disadvantages for

photovoltaic applications: because the ligands are very long insulating molecules, they hinder the charge transport between the PbS NCs [7]. That means that using the nanocrystals with the oleic acid ligands in solar cells would result in poor performance. In order to increase the charge transport, the electronic coupling between the NCs has to improve [13]. When two nanocrystals are brought in close proximity to each other, their wave functions overlap, which increases the electronic coupling between them. This can be done by replacing the oleic acid ligands with a different, shorter molecule. For this purpose 1,4-benzenedithiol (BDT) is used. The ligand exchange takes place after the solution-processing of the PbS layer and in this process the oleic acid ligands are removed and replaced by the BDT molecules [14]. The sulfur atoms in the thiol groups of the BDT molecule form a bond with the lead atoms from the nanocrystal. Since there are two thiol groups for every BDT molecule, this ligand is capable of forming a bond with two NCs, a process that is also called crosslinking [13]. This is depicted in Figure 2.2b.

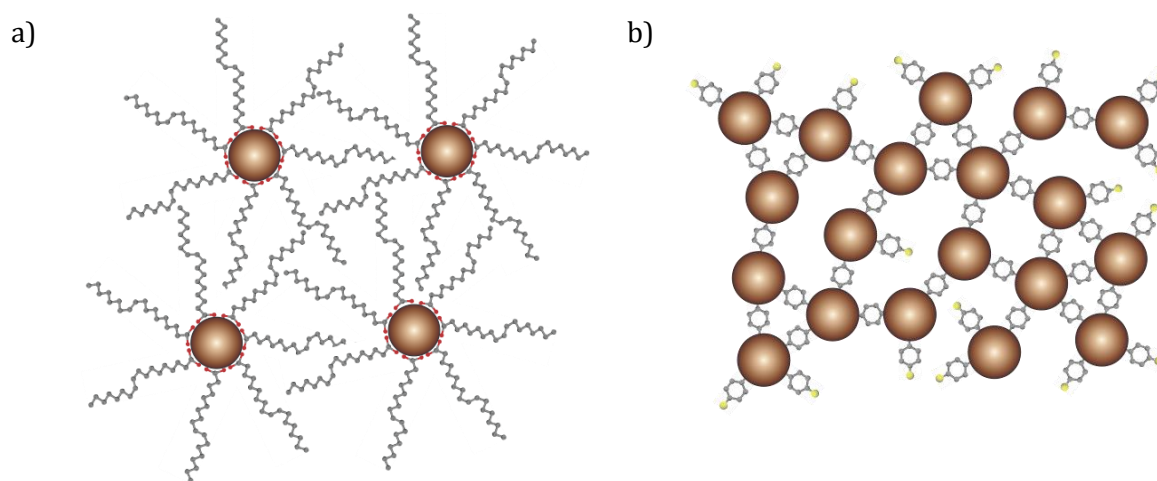


Figure 2.2: Lead sulfide nanocrystals (brown circles) with different ligands. In (a) the ligands are oleic acid and in (b) the oleic acid is replaced with BDT. The BDT molecules are much shorter than the long oleic acid ligands and as a result, the distance between nanocrystals is reduced. The crosslinking process, where two nanocrystals are connected through a BDT molecule, is visible in (b). [6]

## 2.2. Organic semiconductors

The semiconducting properties of organic materials such as polymers originate from the  $\pi$ -bonds between adjacent atomic orbitals in the carbon chain. When two carbon atoms located next to each other undergo  $sp^2$ -hybridization and the atomic orbitals of the two atoms overlap, it will result in a  $\pi$ -bond between the carbon atoms. A so-called conjugated polymer consists of alternating single and double bonds, in which the electrons in the latter are delocalized, enabling them to move and conduct.

Two overlapping atomic  $sp^2$  orbitals can either bond in a constructive way (where the orbitals overlap in-phase) or in a destructive (out-of-phase) way. The former situation leads to a  $\pi$ -bond; the latter to a  $\pi^*$ -bond which is higher in energy, and therefore energetically unfavorable. An electron can be excited from the  $\pi$ -molecular orbital to the  $\pi^*$ -molecular orbital analogous to the excitation from the ground state to an excited state in inorganic semiconductors. In a long conjugated system, the number of  $\pi$ -bonds (and  $\pi^*$ -bonds) is high, leading to a lot of possible transitions. Increasing the number of alternating double bonds leads to a shift of the onset of absorption to higher wavelengths [15]. In the ground state, electrons fill the molecular orbitals

starting from the orbital that is lowest in energy. The highest filled orbital in the ground state is called the Highest Occupied Molecular Orbital (HOMO); the lowest empty orbital is called the Lowest Unoccupied Molecular Orbital (LUMO). These two energy levels are the organic counterparts of the valence and conduction band of an inorganic semiconductor, respectively. The energy difference between the HOMO and LUMO is the band gap of the material.

Charge transport in polymers takes place through the delocalization of electrons in the  $\pi$ -bonds. This allows the charges to hop between states. However, since the intramolecular bonds are much stronger than the van der Waals bonds between molecules, the transport between molecules is low [16]. As a consequence, organic semiconductors have lower charge carrier mobilities than inorganic semiconductors. A widely used polymer such as poly(3-hexylthiophene) (P3HT) has a mobility on the order of  $10^{-1} \text{ cm}^2 \text{ V}^{-1} \text{ s}^{-1}$  [17], whereas inorganic semiconductors can have mobilities on the order of  $10^3 \text{ cm}^2 \text{ V}^{-1} \text{ s}^{-1}$  [18]. In spite of their inferior mobilities, semiconducting polymers have drawn a lot of attention in research. This is due to the fact that the polymers are easy and cheap to process by means of spincoating or inkjet printing, which allows the materials to be used on flexible substrates. This can lead to flexible electronics that can be used in situations where the rigid inorganic devices cannot be employed. In addition, the polymers have a higher absorption coefficient than silicon. This means the films can be made thinner, which reduces the distance that the charges have to travel and partially compensates for the low mobility.

### 2.3 General solar cell

The working principle behind a solar cell consists of three steps: the photogeneration of charge carriers, separation of these carriers (electron and hole) and the extraction of the charge carriers to generate a current over an external load. The photogeneration step takes place when a semiconducting material absorbs a photon with energy  $E_{ph} = \hbar\omega$  (with  $E_{ph} \geq E_G$ ,  $E_G$  being the band gap). The energy of the photon is high enough to excite an electron from the valence to the conduction band, leaving a hole in the valence band. In inorganic semiconductors, the excited electron and the hole are free charge carriers, i.e., they are not bound to each other and are able to move freely. In the case of an organic semiconductor, an exciton will form due to the low dielectric constant of organic materials. This is a bound electron-hole pair with a certain binding energy that needs to be overcome in order for the electron and hole to become free charge carriers. The binding energy is bigger than the thermal energy  $kT$  at room temperature. The difference between organic and inorganic solar cells will be explained in more detail in the section on organic solar cells and the current section will focus on the basic photovoltaic concepts of inorganic p-n junctions. After the charge carriers have been generated, they have to be separated. This is done by applying an electric field over the solar cell. Every solar cell has a built-in potential that enables the drift of the charge carriers across the device. In inorganic p-n junction solar cells the electric field is due to the combination of n-type and p-type semiconducting materials. For organic solar cells the built-in potential is caused by the difference in work function of the cathode and anode [19]. When the charge carriers are transported through the device due to the built-in electric field they can be extracted at the electrodes: the electron at the cathode and the hole at the anode.

A p-n junction is a semiconducting material with two distinct regions: one of which is n-type doped (i.e., the majority of free charge carriers are electrons) and the other one is p-type doped (the majority carriers are holes). The diffusion of the charge carriers (the electrons in the n-type material going to the p-type region and the holes in the p-type material to the n-type region) leads to a third region at the junction where the holes and electrons recombine. As a result, this region has no free charge carriers. On both sides of this so-called depletion region the majority carriers are reduced in numbers, which leads to ionized donors in the n-type region and to ionized acceptors in

the p-type region. This buildup of charge on both sides leads to a built-in electric field across the depletion region which inhibits the diffusion of charge carriers. Without applying an external electric field there will be an equilibrium between drift and diffusion and as a result no net charge will flow through the device (see Figure 2.3) .

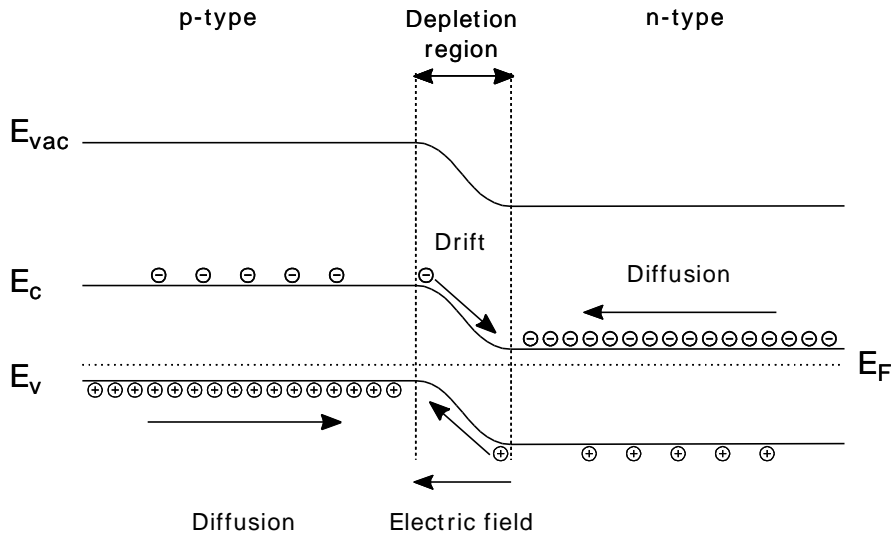


Figure 2.3: Energy band diagram of a p-n junction in equilibrium, without an external bias. The built-in electric field balances out the diffusion current and as a result no net current flows.  $E_{VAC}$  is the vacuum energy level,  $E_F$  is the Fermi level and  $E_C$  and  $E_V$  are the energy levels of the conduction and valence band, respectively.

Applying an external bias voltage over the device can result in two situations: a large current flowing through the p-n junction if the voltage is applied in the so-called forward direction, or a small current flowing through the device when the bias voltage is applied in the reverse direction. These directions are defined as follows: in the forward direction, a positive potential is applied to the p-type region relative to the n-type region. This leads to an electric field which is opposite to the internal electric field in the depletion region and the electric field hindering the diffusion is lowered (Figure 2.4a). The reverse direction is defined with an opposite external electric field, i.e., a negative potential is applied to the p-type region relative to the n-type region. Therefore, this field has the same direction as the built-in electric field and the net electric field increases, which hinders the diffusion of charge carriers across the depletion region (Figure 2.4b). In fact, the diffusion current is negligible and the current is determined by the drift current of minority carriers into the p-side or n-side for holes and electrons, respectively. This current is much smaller than the total current in the forward direction, which gives the diode the unique property of only conducting in one direction. The diode behavior can be described by the diode equation (Equation 2.1)

$$I_D = I_0(e^{\frac{qV}{nkT}} - 1) \quad (2.1)$$

where  $I_D$  is the net diode current,  $I_0$  the leakage current,  $q$  the elementary charge,  $n$  the ideality factor of the diode,  $k$  is Boltzmann's constant, and  $T$  the absolute temperature in kelvin. For an ideal diode  $n$  is equal to 1. A typical example of the current density-voltage characteristics of a diode is shown in Figure 2.5, where the current density is the current per unit area.

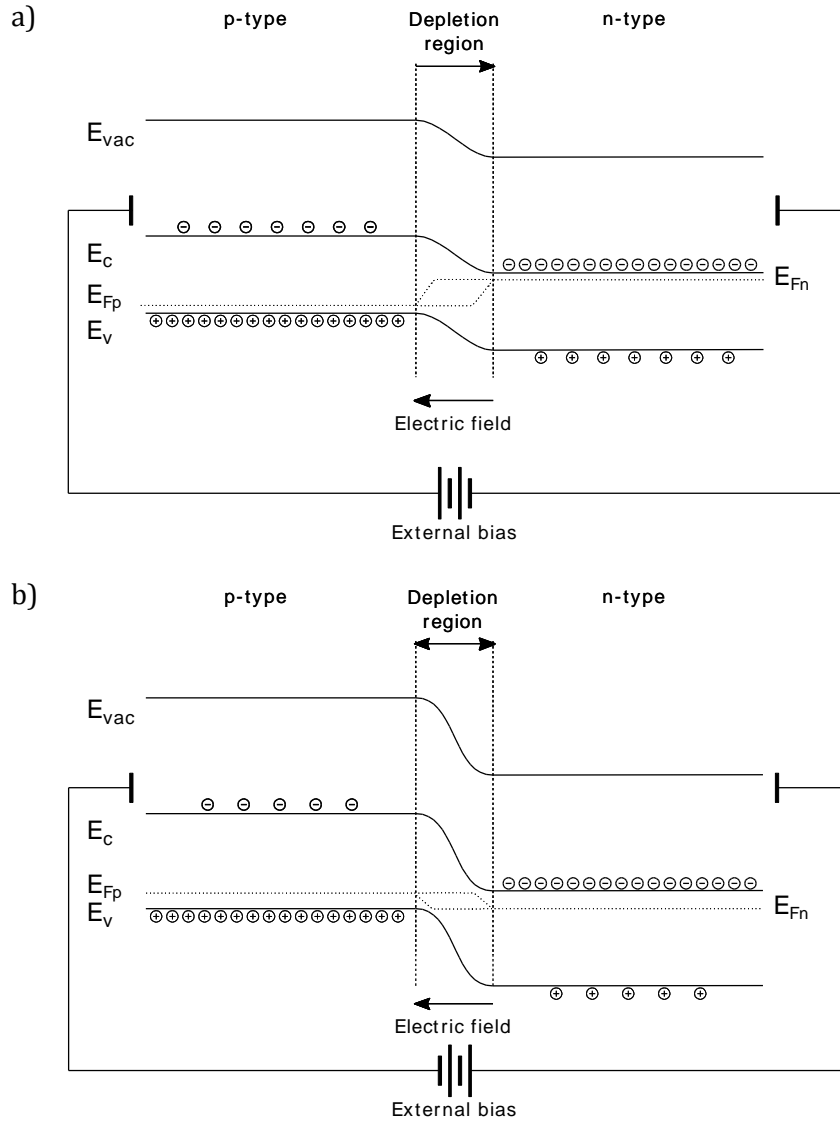


Figure 2.4: The p-n junction under (a) forward bias and (b) reverse bias. For the forward bias case, an external bias is applied with the positive terminal connected to the p-type side and the negative terminal to the n-type side. In the case of the reverse bias, the polarity of the external bias is reversed.

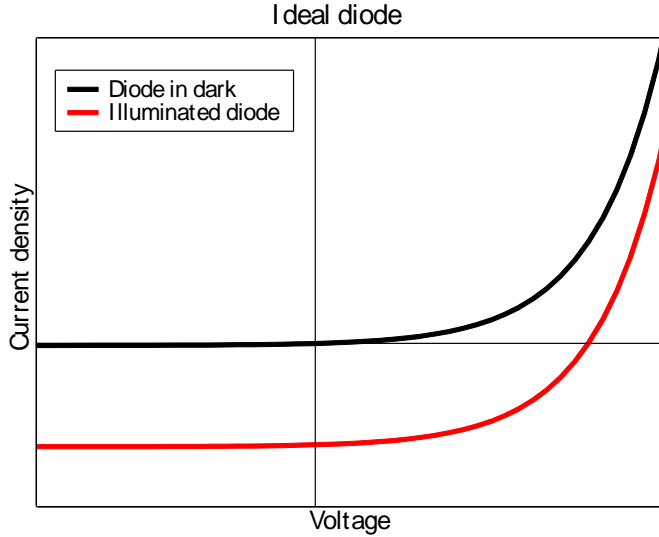


Figure 2.5: Current density-voltage characteristics of an ideal diode in the dark (see Equation 2.1) and under illumination (Equation 2.2).

When the p-n junction is illuminated, there will be photons striking the semiconducting material. A photon with an energy equal to or bigger than the band gap of the semiconductor can be absorbed and converted into an electron-hole pair. Since the layer with the semiconducting regions converts the light to electric charges, it is called the active layer. The region where the photogeneration takes place determines which charge carrier is the majority and the minority carrier. The minority charge carrier can exist for a certain time before it recombines with the majority carrier; this is called the lifetime of the minority carrier. In the case of recombination the photocurrent is lost. When the minority carrier can diffuse to the depletion region within its lifetime, it can be saved from recombination. The average distance it can travel within its lifetime is called the diffusion length. An electron-hole pair generated at a distance from the depletion region which is smaller than the diffusion length can contribute to the photocurrent. The minority carrier is swept across the depletion region due to the electric field and becomes a majority carrier in the other region. Both regions have an ohmic contact with a (metal) electrode and when the charges diffuse to the electrodes they can be extracted, resulting in a current. Since the light-generated current  $I_L$  flows against the external electric field, it carries a negative sign and this is introduced into the diode equation as can be seen in Equation 2.2.

$$I = I_0 \left( e^{\frac{qV}{nkT}} - 1 \right) - I_L \quad (2.2)$$

A typical current density-voltage (J-V) curve of a p-n junction under illumination (a solar cell) is plotted in Figure 2.5. The dark diode curve is shifted downwards when the solar cell is illuminated. There are two intersections with the axes: one where  $V$  is zero and the other where  $J$  is zero. These two points are called the short-circuit current density ( $J_{sc} \equiv J(V=0)$ ) and the open-circuit voltage ( $V_{oc} \equiv V(J=0)$ ), respectively. They play an important role in the characterization of solar cells, as will be explained later. In the case of short-circuit, the diffusion of charges across the depletion region is hindered and the major contribution to the current comes from the drift of the photogenerated minority carriers. In the case of an open-circuit, the applied electric field is equal in magnitude but opposite in sign to the built-in voltage. At this point, the photogenerated current cancels out the diffusion current and no net current flows. In between the short-circuit and open-circuit points, the current is located in the fourth quadrant of the graph. It is possible to generate power from this

quadrant and the magnitude of the power is determined by the product of the current and voltage. As one increases the bias over the solar cell from zero to the open-circuit voltage, the current density decreases in magnitude and it is clear that somewhere in the fourth quadrant there is a maximum value for the power at the so-called Maximum Power Point (MPP):

$$P_{MPP} = V_{MPP} \cdot J_{MPP} \quad (2.3)$$

The fill factor ( $FF$ ) is used to characterize the shape of the JV curve between  $J_{SC}$  and  $V_{OC}$ . Its definition is given in Equation 2.4 and an illustration is shown in Figure 2.6. Here, the ratio of the area of the ideal solar cell in the fourth quadrant that is covered by the blue rectangle is the fill factor.

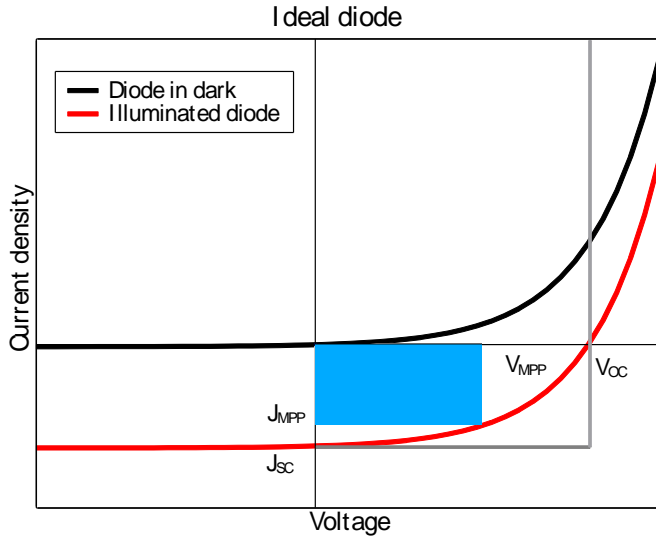


Figure 2.6: Current density - voltage ( $J$ - $V$ ) curves of a diode under dark conditions and an illuminated diode. The blue rectangle shows the maximum power that can be extracted from the device plotted in red.

$$FF = \frac{P_{MPP}}{V_{OC} \cdot J_{SC}} = \frac{V_{MPP} \cdot J_{MPP}}{V_{OC} \cdot J_{SC}} \quad (2.4)$$

The maximum power  $P_{MPP}$  is also called the power conversion efficiency  $\eta$  of the solar cell. By definition, following from Equation 2.4, the power conversion efficiency (PCE) is given by:

$$\eta = \frac{V_{OC} \cdot J_{SC} \cdot FF}{P_{in}} \quad (2.5)$$

where  $P_{IN}$  is the intensity of the incident light. The evaluation of solar cells is usually done by listing the values for  $V_{OC}$ ,  $J_{SC}$ ,  $FF$  and  $\eta$ , along with plotting the  $J$ - $V$  curve. This is important because each parameter gives information about the device and about how its performance might be improved.

## 2.4 Non-ideal solar cell

The behavior of a real solar cell deviates from the ideal case, and can be modeled using an equivalent circuit model, shown in Figure 7. In the ideal case, the external load is powered by the current coming from the diode and a current source, which represents the contribution from the photocurrent  $I_L$ . The non-ideal circuit has two additional resistors: one parallel to the diode called the shunt resistance  $R_{SH}$ , and the other one is in series and is therefore called the series resistance  $R_S$ . These two resistors lead to a new equation for a non-ideal solar cell (Equation 2.6). The current flowing through the shunt resistance represents the current loss through leakage (e.g., when an alternative path for the current exists) in the device. Ideally, the shunt resistance should be infinite. When the shunt resistance is low, the voltage and fill factor of the device decrease.

$$I = I_0 \left( e^{\frac{q(V+IR_S)}{nkT}} - 1 \right) - \frac{V + IR_S}{R_{sh}} - I_L \quad (2.6)$$

The series resistance of the solar cell is due to the non-zero resistivity of the materials that are used in the cell and the contact resistance at the interfaces of the materials. It hinders the current flowing through the device and lowers the fill factor. In the ideal case the series resistance is zero. The two resistances represent factors that account for energy loss, such as recombination due to surface and bulk traps. These traps are states that are lower in energy than the free charge carriers, i.e., they lie in the band gap of the semiconductor. A charge carrier that comes across a trap will occupy this lower energy state and loses its mobility. When an opposite charge carrier moves to the trap site both charge carriers recombine.

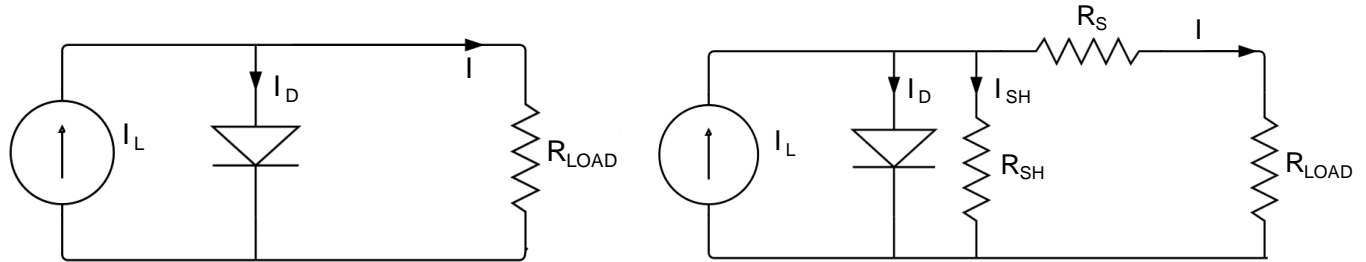


Figure 2.7: Equivalent circuits of an ideal solar cell (left) and a non-ideal solar cell (right). The current source represents the photocurrent,  $I_D$  is the current through the diode and  $I$  is the total current through the device. An external load is simulated by adding a resistor to the diagram. In the non-ideal case the parasitic shunt and series resistances are included as  $R_{SH}$  and  $R_S$ , respectively.

Another source of energy loss stems from the band gap of the semiconductor. When a photon with an energy higher than the band gap energy hits the solar cell it can be absorbed and it creates an electron-hole pair. The electron is excited to the conduction band, where the energy in excess of the band gap energy is initially given to the electron as kinetic energy but quickly dissipates as heat through phonon interactions. This means that all the photons with a wavelength lower than the wavelength of the absorption onset are not used to their full potential. However, having a very large band gap (and thus absorption onset from a low wavelength) reduces the portion of the solar spectrum that can be absorbed (see Figure 2.8). This indicates that there is a delicate balance between band gap and the maximum power that a solar cell can deliver. According to a model by Shockley and Queisser, the detailed balance limit for the efficiency of a single junction solar cell is about 30%, and can be reached with a semiconductor that has a band gap of 1.1 eV [20]. Despite this upper limit, it is still possible to increase the efficiency of solar cells over 30%. One approach for this is using a tandem solar cell, in which two materials are used with a complementary absorption spectrum, i.e., they have different band gaps. The detailed balance limit for a tandem

solar cell with two subcells is 42.7%. In order to reach this efficiency, the band gaps of the subcells need to be equal to 1.0 and 1.9 eV [21]. As already described above, the lead sulfide nanocrystals have a tunable band gap, making them an ideal material for the tandem solar cell. They can be combined with the aforementioned organic semiconductors to cover a wide range of the solar spectrum. In order to understand the tandem solar cell one first needs to be familiar with the individual subcells of the tandem cell. The next two sections will introduce the nanocrystal and organic solar cells.

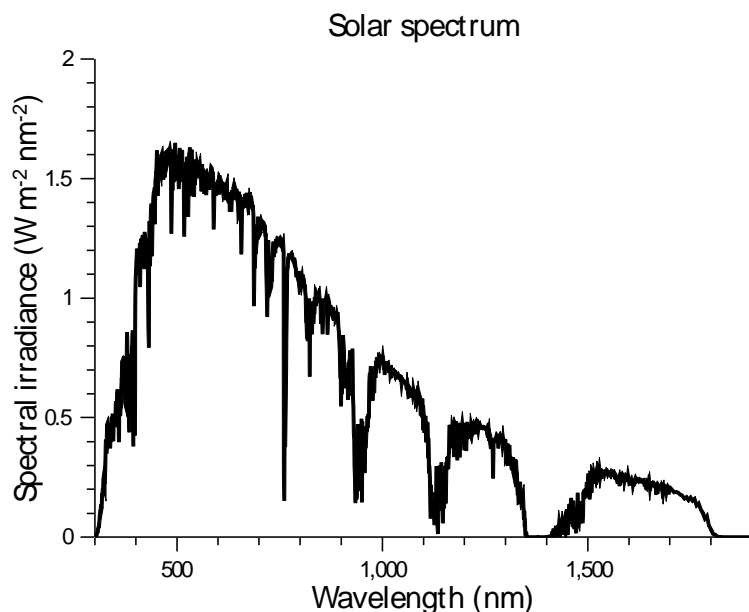


Figure 2.8: The spectral irradiance of the solar spectrum (AM1.5G).

## 2.5 PbS nanocrystal solar cells

The first use of PbS nanocrystals in photovoltaic cells dates back more than twenty years [22]. Initially, the lead sulfide was used as a sensitizer in a dye-sensitized solar cell structure. In the meantime, more cell structures have been used to exploit the unique optical and electrical properties of the NCs. The most commonly used structures are the Schottky cell [23], the planar heterojunction [24] and the bulk heterojunction solar cell [25]. The latter two device architectures use the nanocrystals in combination with another material such as PC<sub>60</sub>BM in the planar heterojunction, or polymers in the case of the bulk heterojunction. However, these structures were not used for the nanocrystal solar cells in this work and therefore only the Schottky cell will be introduced here. The other two device architectures will be explained more in-depth in the following section on organic solar cells.

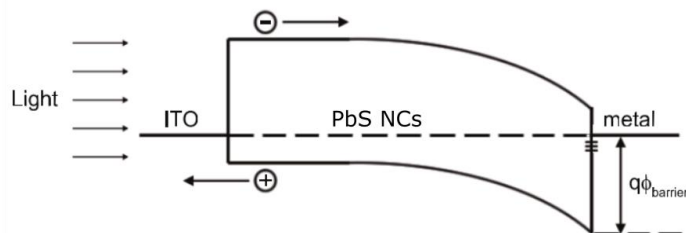


Figure 2.9: Schematic diagram of a lead sulfide nanocrystal Schottky solar cell. The band bending at the PbS – metal interface leads to the formation of the Schottky barrier. [13]

The Schottky solar cell is depicted in Figure 2.9. It has a semiconductor (the PbS NCs) in contact with a metal electrode. In equilibrium, the charges diffuse so that the Fermi levels of the two materials align. At the junction, there is a depletion layer analogous to the p-n junction. The valence and conduction band of the semiconductor bend due to the alignment of the Fermi levels, which forms a barrier at the interface that restricts the flow of holes to the metal. Depending on the height of the barrier, the contact between the semiconductor and metal can be ohmic or non-ohmic. An ohmic contact requires low resistance and therefore a low Schottky barrier. When the barrier is high, a non-ohmic contact forms. In Figure 2.9 one can see that there is a second junction in the Schottky solar cell. This is between the PbS and indium tin oxide (ITO), a transparent conducting oxide electrode. Here, the bands bend less than at the PbS-metal junction [13]. The creation of the Schottky barrier results in the diode-like properties of this particular device. Photocurrent can be generated upon illuminating the Schottky cell, analogous to the p-n junction.

The absorption of light by the lead sulfide solar cell can be adjusted by changing the size of the nanocrystals. This opens up the possibility of tuning the band gap to make it equal to that of silicon (1.1 eV), which is the ideal value according to Shockley and Queisser. For a PbS NCs Schottky solar cell this can result in a power conversion efficiency of 5.2%, with a  $J_{SC}$  of 19.3 mA/cm<sup>2</sup>, a  $V_{OC}$  of 0.46 V and a fill factor of 58% [23]. In this case, the excitonic peak is located at around 1100 nm (Figure 2.10) and a large portion of the light from the solar spectrum can be absorbed which leads to the high value for the short-circuit current density. In addition to this, there is another property of the lead sulfide nanocrystals that leads to an increase in  $J_{SC}$ : multiple exciton generation (MEG). In this process, the absorption of one photon leads to the formation of multiple electron-hole pairs. For this to happen, the photon needs to have an energy that is much higher than the band gap energy  $E_G$  [26]. After absorbing the high-energy photon, an electron can be excited to the conduction band and the excess energy of the photon can be transferred to the electron as kinetic energy. If this electron encounters a bound electron, it can transfer its energy and free the other electron in a process called impact ionization. Ellingson et al. found that PbS NCs ( $E_G = 0.85$  eV) can produce almost three excitons when the photon energy  $E_{hv}$  is four-and-a-half times the band gap energy [26]. Theoretically, this means that the Shockley-Queisser limit could be exceeded by PbS NC solar cells. One of the factors that prevents this is the open-circuit voltage of the solar cells. The absorbance indicates that the band gap of the nanocrystals should be around 1.1 eV and the value for the open-circuit voltage is merely half of this. This is typical for nanocrystal solar cells; most cells do not have a  $V_{OC}$  higher than about 0.5  $E_G$ . The origin of this loss stems from surface defects states on the crystals [27]. When these mid-gap states are filled the splitting of the quasi-Fermi levels of electrons and holes is reduced, leading to a lower open-circuit voltage. The surface defects can originate from the ligand exchange (from oleic acid to BDT), for example, when there are dangling bonds present which do not have a ligand to bind to [13]. This problem can be solved by passivation of the surface traps, e.g., by using small ligands to bind to the defects [28].

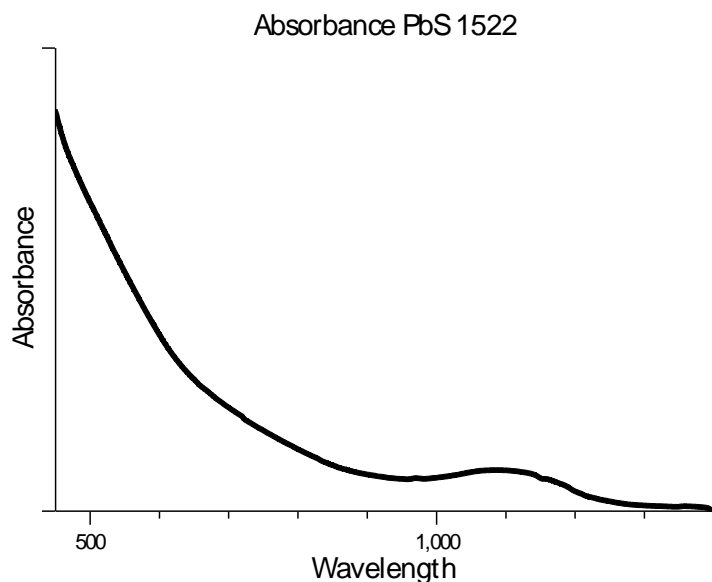


Figure 2.10: The absorbance spectrum of lead sulfide nanocrystals (batch PbS 1522). The excitonic peak can be seen around a wavelength of 1100 nm. The onset of absorption is located around 1300 nm.

## 2.6 Organic solar cells

Organic solar cells, made from either polymers or small molecules, differ a lot from their inorganic (silicon) counterparts. One of the major differences between them is that the latter are more expensive to make. Other differences include: difference in weight (polymers are lighter than inorganics) and low environmental impact [29]. Another advantage of using organic solar cells is the high absorption coefficient of the organic semiconductors. This leads to a high optical density for films with thicknesses smaller than 100 nm [16], whereas thin film silicon solar cells have thicknesses in the range of micrometers [30]. As a result, less material is needed for the production. Another fundamental difference between inorganic and organic cells is that in the former, charge separation occurs throughout the bulk of the material when a photon is absorbed and promotes an electron from the valence band to the conduction band. However, in organic solar cells the absorbed photon creates an exciton due to the low dielectric constant ( $\epsilon = 2-4$ ) of polymers [31]. This low dielectric constant leads to a strong bonding between the electron and the hole, with a significant binding energy that has to be overcome in order to separate the charges.

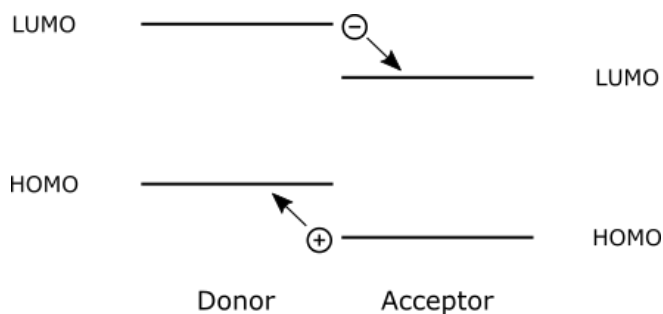


Figure 2.11: A schematic representation of a type II heterojunction with a donor and an acceptor. Due to the position of the HOMO and LUMO levels in both materials, the electron goes to the acceptor and the hole to the donor. This mechanism is the basis of exciton dissociation in organic solar cells.

Unlike the inorganic p-n junction, which consists of two regions of semiconductors with different doping, the active layer of the organic solar cells is made of two different semiconductors: one being the electron donor and the other the electron acceptor. Polymers (e.g. P3HT) act as the donors and the electron acceptors are typically fullerene derivatives such as phenyl-C61-butyric acid methyl ester (PC<sub>60</sub>BM). In order to separate charges at a donor-acceptor interface, the HOMO and LUMO levels of the donor need to be higher than the HOMO and LUMO levels of the acceptor, respectively. This is called a type II heterojunction (see Figure 2.11). There are two kinds of type II heterojunctions: the planar and the bulk heterojunction. The former is shown on the left in Figure 2.12 and consists of a donor layer and an acceptor layer stacked on top of each other. In this case the performance of the solar cell is not very good since charge separation can only occur at the donor-acceptor interface and this area is limited [29]. A bulk heterojunction consists of a mixed layer of donor and acceptor domains and is shown on the right in Figure 2.12. In this situation the total interface area is a lot bigger, therefore more charge separation is possible. For this thesis only bulk heterojunctions were used because the overall performance of these heterojunctions is better than for planar devices. This results from the diffusion length of the excitons in the materials. The diffusion length is the average distance over which the exciton can diffuse before it relaxes back to the ground state and for most organic materials this length is about 3 to 15 nm [32]. If the domain sizes in the bulk heterojunction are larger than the diffusion length the exciton will recombine and no charge will be extracted. Besides these losses, there is also a loss mechanism that occurs when the exciton manages to diffuse to a donor-acceptor (D/A) interface: the recombination of electrons and holes at the interface. Recombination of an electron-hole pair coming from a single photon is called geminate recombination and both mechanisms discussed above belong to this category. Another loss mechanism is the so-called non-geminate recombination, where the separated charge carriers encounter an opposite charge carrier that does not come from the same photon. An example of this type of recombination is trap-assisted combination, in which a mobile charge carrier recombines with an oppositely charged trapped carrier [33].

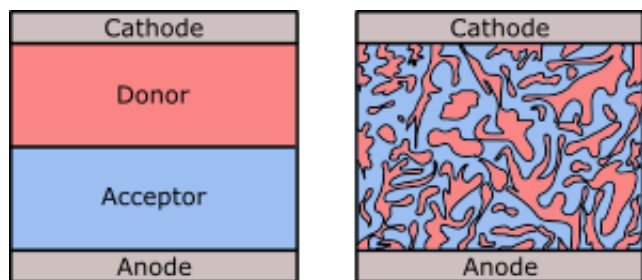


Figure 2.12: Schematic illustrations of a planar heterojunction (left) and a bulk heterojunction (right), consisting of a polymer (donor) and fullerene (acceptor).

For organic solar cells, the built-in electric field driving charge transport originates from the difference in the work functions of the metal electrodes [34]. In the absence of an external bias, no net current flows until the solar cell starts to absorb light; the same condition as for the p-n junction. Applying an external bias will result in reverse and forward bias conditions equivalent to the inorganic case. The transport of charge carriers has to take place through percolation pathways since there are distinct domains of donor and acceptor regions. In order to reach the respective electrodes a path needs to be present from the D/A interface to the electrode within the donor and acceptor for the holes and electrons, respectively. This shows the importance of having a good morphology of the polymer and fullerene, with percolation pathways in addition to a large number

of D/A interfaces. Changing the processing conditions of the polymer-fullerene blend means that the morphology can be influenced.

## 2.7 Tandem solar cells

There is a dilemma that one encounters when trying to increase the thickness of the active layer of a single solar cell: the higher thickness leads to more light absorption, i.e., more photocurrent, but increasing the thickness beyond the diffusion length of the charge carriers will degrade the efficiency of the solar cell due to increased recombination. In addition, the series resistance of the device will be higher with increasing thickness, which in turn leads to a reduced  $V_{oc}$  and  $FF$  [35]. Using a tandem structure circumvents this problem. A tandem solar cell consists of two subcells connected in series through a layer which is called the interlayer (see Figure 2.13a). Each subcell is a solar cell on its own, with an active layer placed between an anode and a cathode. Here, the thicknesses of both subcells can be optimized with regard to absorption and recombination. However, there is still a trade-off present in the tandem cell; a major constraint is the need for current matching in the subcells. When one of the subcells produces more current than the other, then this surplus is lost. This phenomenon will be explained later in this section.

In order to make an electrical connection between the two subcells, the interlayer has to consist of an anode and a cathode (Figure 2.13b). Kirchhoff's law dictates that the short-circuit current density of the tandem cell is determined by the lowest current of the two subcells:

$$J_{Sc_{total}} = \text{Min}(J_{Sc1}, J_{Sc2}) \quad (2.7)$$

where  $J_{Sc1}$  and  $J_{Sc2}$  are the short-circuit current densities of the subcells. The total open-circuit voltage of the tandem equals

$$V_{Oc_{total}} = V_{Oc1} + V_{Oc2} \quad (2.8)$$

Here,  $V_{Oc1}$  and  $V_{Oc2}$  are the open-circuit voltages of the subcells. This is the result of connecting the subcells in series.

Ideally, the tandem solar cell is made of two semiconducting materials with complementary absorption spectra, that is, they have no overlapping absorption. In this case the front cell does not absorb any light that the back cell can also convert to electricity and both subcells can be optimized individually to match the current. In practice, realizing complementary absorption can be difficult. When there is an overlap between the two absorption spectra, it is a good strategy to make the wide band gap subcell the front cell and use the smaller band gap material in the back cell. This prevents that most of the light with lower wavelengths is absorbed by the low band gap material, leaving virtually no light for the other material to absorb. This would result in a very low  $J_{sc}$  and PCE for the tandem.

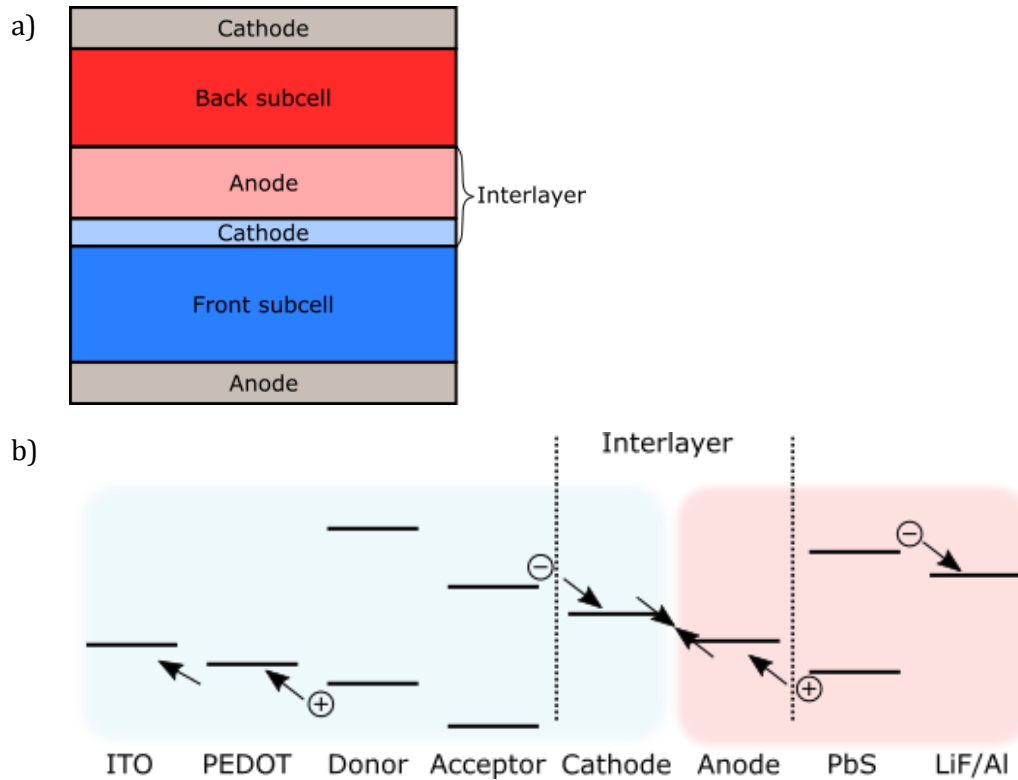


Figure 2.13: (a) A schematic representation of a tandem solar cell. The interlayer, which consists of a cathode and an anode, is inserted between the front and back subcell. In this thesis, the active material of the front subcell is a polymer-fullerene blend and for the back subcell this is a PbS NC layer. A general energy level diagram of the polymer-PbS tandem cell is depicted in (b). The function of the interlayer is visualized here. The electrons from the front subcell (highlighted in blue) are transported to the cathode of the interlayer, where they recombine with the holes from the back subcell (highlighted in red). This recombination is necessary to prevent the build-up of charges in the device. Energy levels are not to scale.

Another prerequisite for good photovoltaic performance of a tandem cell is having a suitable interlayer between the two subcells. The ideal interlayer meets three requirements, one of which is optical transparency. The light that passes through the front cell should not be absorbed by the interlayer before it reaches the back cell, because this would result in a lower photocurrent. Furthermore, the interlayer has to act as a recombination site for the electrons coming from the front cell and the holes from the back cell. In the perfect case the number of holes and electrons in the interlayer are equal and all the charge carriers recombine. However, when there is an imbalance in the charge carrier densities there will be a build-up of charge in the interlayer which opposes the built-in electric field of the subcell causing the imbalance. As a result, the current in this subcell is lowered until there is current matching between the subcells [36]. In order to extract the charges from both subcells efficiently, the contact between a subcell and the interlayer needs to be ohmic. The third requirement for an interlayer is that it is a protective layer for the front subcell during device processing. When the back subcell is made by a solution-processing technique it is possible that the selected solvent might be capable of dissolving the active layer material from the front cell. In order to prevent this, the interlayer needs to be uniform, that is, there should be no cracks or holes present in the layer through which the solvent could penetrate. It is also required that the interlayer does not dissolve in this solvent for the same reason.

Another factor that comes into play during the design of the interlayer is the optical spacer effect. The optical electric field that is present in a solar cell under illumination is influenced by absorption, reflection at the interfaces and interference. It has several maxima and minima throughout the solar cell with corresponding high or low light intensity (see Figure 2.14). For a solar cell it is ideal to have a maximum of the optical electric field located in the active layer for generating the highest photocurrent. However, the previously mentioned reflection and interference may lead to a non-ideal situation. An example is destructive interference caused by the reflection of light by the metallic back contact (Al) [37], which decreases the light intensity at that location. In order to prevent this, an additional layer can be inserted in the solar cell, a so-called optical spacer. Gilot et al. used ZnO for this purpose because of its high optical transparency [38]. The effect is that the optical electric field is redistributed and a maximum of the field is now located in the active layer. This shows the importance of selecting the right thickness for each layer, which can be determined by optical simulations. For this, a model of the solar cell's optical properties is needed. This will be explained in the experimental chapter.

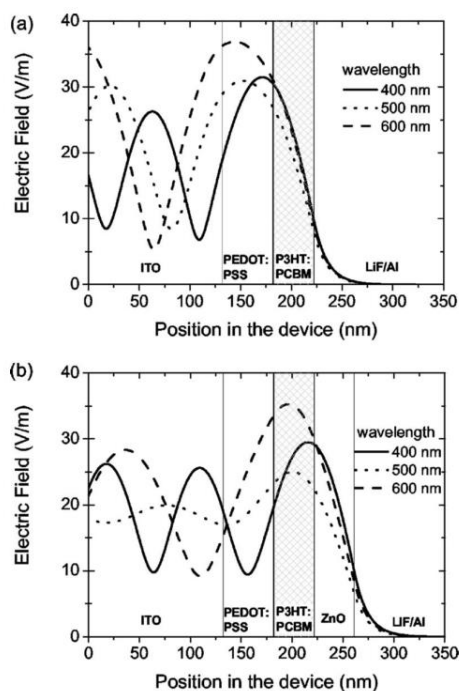


Figure 2.14: Distribution of the optical electric field in a solar cell (a) without and (b) with optical spacer (ZnO) for light with different wavelengths. [38]

Tandem solar cell structures have been used extensively for organic materials [36, 39, 40], which has led to a power conversion efficiency of 10.6% [5]. However, this cell only absorbs light with wavelengths smaller than 900 nm, and therefore it does not make use of the infrared part of the solar spectrum. PbS nanocrystals can be used in a tandem to cover the IR part of the spectrum and this was done by Wang et al. in 2011 [41]. They used the lead sulfide NCs in both subcells, where the NCs in the front cell had a higher band gap (1.6 eV) than the NCs in the back cell (1 eV). This enabled the cell to absorb light with wavelengths up to 1400 nm, resulting in a PCE of 4.2%. Nevertheless, the overlap of absorption spectra between the NCs is large and this is a non-ideal situation for a tandem solar cell. The absorbance of the nanocrystals is high in the ultraviolet region and a material that is complementary in absorption should therefore only absorb in the visible, where the absorbance from the PbS is relatively low. Polymers such as P3HT are an excellent

candidate because they mainly absorb in the visible part of the optical spectrum. Our group was the first to combine PbS NCs with polymers in a tandem solar cell [6], which led to a 1.8% PCE cell with 92% of the sum of the subcell  $V_{oc}$ 's. The tandem cell had a configuration where the active layer of the front cell consisted of PbS NCs and the back cell of P3HT:PCBM. This not the most favorable for the tandem since the lower band gap material is in the front and the back cell is illuminated with a lower light intensity. However, it also has advantages to use this approach. The lead sulfide in the front cell will absorb most of the UV light impinging on the solar cell, so it does not reach the polymer. This reduces the photo-oxidation (the degradation of polymer solar cells when they are illuminated with ultraviolet light in the presence of oxygen) [42]. Moreover, the processing of the tandem is easier for this configuration since crosslinking the PbS NCs makes them practically insoluble in the solvent used for the back solar cell, in case the interlayer does not fully shield the front cell from the solvent. Despite this, it is more favorable for the power conversion efficiency to use the tandem configuration where the polymer is in the front. It is mentioned in the paper that theoretically the  $J_{sc}$  of the tandem cell could be  $9.5 \text{ mA/cm}^2$ , instead of  $3.9 \text{ mA/cm}^2$  for the current configuration. The next chapter will describe the materials used in this tandem configuration.

## Chapter 3 Materials

The polymer-lead sulfide nanocrystal tandem solar cell consists of several layers, as can be seen in Figure 2.13a. Each of these layers is made with different materials. For a good understanding of the structure of the tandem solar cell it is essential to examine the individual layers carefully. For this reason, the materials that have been used in the processing of the solar cells are described in this chapter.

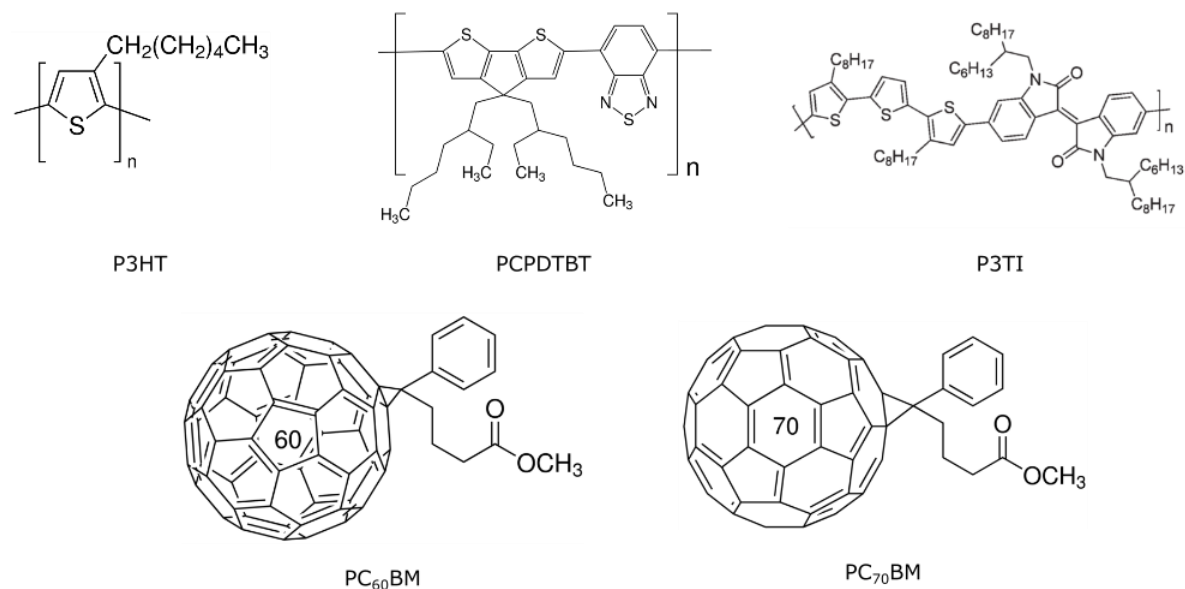


Figure 3.1: The structural formulas of the polymers (top row) and the fullerenes (bottom row) used in this thesis.

### 3.1 P3HT

The polymer poly(3-hexylthiophene) (P3HT) is one of the most studied polymers in research on organic solar cells. The structural formula of P3HT is given in Figure 3.1. In the organic solar cells it acts as an electron donor with a band gap of 1.9 eV. Its HOMO and LUMO levels are located at -5.1 eV and -3.2 eV, respectively [35]. P3HT is used in a bulk heterojunction in combination with PC<sub>60</sub>BM (also called PCBM), which acts as the electron acceptor. Efficiencies of solar cells with this active layer have reached values up to 5% (with a  $V_{oc}$  of 0.61 V, a  $J_{sc}$  of 11.1 mA/cm<sup>2</sup> and a fill factor of 0.66) [43]. The bulk heterojunction of P3HT:PCBM is made by solution processing. In this process the solutes are dissolved in 1,2-dichlorobenzene (or orthodichlorobenzene, ODCB). This solvent has a high boiling point of 183°C, which is beneficial for the morphology of the layer since a high boiling point solvent evaporates slowly, leading to a highly ordered film [44].

### 3.2 PCPDTBT

Poly[2,6-(4,4-bis-(2-ethylhexyl)-4H-cyclopenta [2,1-*b*;3,4-*b'*]dithiophene)-*alt*-4,7(2,1,3-benzothiazole)], or PCPDTBT, is a low band gap polymer ( $E_g = 1.4$  eV). Figure 3.1 displays the structural formula of this polymer. The HOMO and LUMO levels are -4.9 eV and -3.5 eV, respectively [35]. Due to the low band gap energy, the polymer absorbs light with wavelengths up to 900 nm. PCPDTBT is used in combination with PC<sub>60</sub>BM in bulk heterojunctions. In order to enhance the carrier lifetime in the layer, Peet et al. used the additive 1,8-octanedithiol (ODT). This additive improves the morphology of the heterojunction, leading to a higher current density and fill factor [45]. As a result

of the use of the additive and the broad absorption, PCPDTBT can generate more photocurrent than P3HT and this is evident from the  $J_{sc}$  which equals 16.2 mA/cm<sup>2</sup>. The power conversion efficiency obtained by Peet et al. equaled 5.5%. The active layer of PCPDTBT with PCBM is made from a solution in chlorobenzene.

### 3.3 P3TI

The third polymer that was used for this research is poly[N,N'-bis(2-hexyldecyl)isoindigo-6,6'-diyl-alt-thiophene-2,5-diyl] (P3TI). The first paper on this polymer was published in 2011, where it was used in solar cells giving 6.3% PCE [46]. It has a band gap of around 1.5 eV; experimentally the HOMO and LUMO levels were found to be -5.7 eV and -4 eV [47]. It is used in combination with PC<sub>70</sub>BM as the electron acceptor. These materials are dissolved in orthodichlorobenzene for the solution processing. When this solution is used the resulting film has large PC<sub>70</sub>BM domains and in order to prevent this 1,8-diiodooctane (DIO) is used as an additive, which decreases the size of the domains [46]. Ma et al. used the solution with additive in their solar cells which resulted in 6.9% efficiency [47]. In particular the high  $V_{oc}$  (0.72 V) and  $J_{sc}$  (14.6 mA/cm<sup>2</sup>) of this solar cell are interesting for the polymer-PbS tandem structure under investigation.

### 3.4 PC<sub>60</sub>BM

In order to achieve charge separation in the bulk heterojunction, the polymers mentioned above need to be in contact with electron acceptors. The most used acceptor in organic solar cells is [6,6]-phenyl-C<sub>61</sub>-butyric acid methyl ester (PC<sub>60</sub>BM) (see Figure 3.1). This is a derivative of the C<sub>60</sub> Buckminsterfullerene and due to its high electron mobility and electronegativity it is well suited as acceptor material [48]. PCBM is soluble in organic solvents such as ODCB which enables dissolving the polymer and PCBM in the same solvent [49]. The HOMO level is -6.1 eV and the LUMO level is -4.3 eV, making the band gap 1.8 eV [35].

### 3.5 PC<sub>70</sub>BM

An alternative to PC<sub>60</sub>BM is the C<sub>70</sub> equivalent: [6,6]-phenyl-C<sub>71</sub>-butyric acid methyl ester, or PC<sub>70</sub>BM. The structural formula of this material is depicted in Figure 3.1. The main advantage of using PC<sub>70</sub>BM over PC<sub>60</sub>BM in a solar cell is that the former has increased absorption in the visible range of light which can increase the  $J_{sc}$  [50]. The HOMO and LUMO levels are the same as for PC<sub>60</sub>BM (-6.1 eV and -4.3, respectively) [35]. A downside to PC<sub>70</sub>BM is that the electron mobility of the material is three times lower than that of PC<sub>60</sub>BM ( $6.8 \times 10^{-4}$  cm<sup>2</sup> V<sup>-1</sup> s<sup>-1</sup> versus  $2 \times 10^{-3}$  cm<sup>2</sup> V<sup>-1</sup> s<sup>-1</sup>). This can result in a build-up of charge when it is used in combination with a polymer with a higher hole mobility, leading to a lower fill factor [50]. When selecting an acceptor for a bulk heterojunction, one has to take this trade-off into account and investigate which fullerene results in the best performance.

### 3.6 PbS nanocrystals

The lead sulfide nanocrystals used for this thesis are colloidal solutions in chloroform. After the NCs are synthesized they are dissolved in toluene since they are more stable in this solvent. For the solution processing the solvent is replaced by chloroform, which has a higher vapor pressure than toluene. This means that it is more volatile and this is favorable for the layer formation [51]. The nanocrystals in the chloroform are capped with the long, insulating oleic acid ligands and the resulting film suffers from poor charge transport. As described in the theory, the ligands can be replaced with 1,4-benzenedithiol (BDT, dissolved in acetonitrile) to increase the charge transport by reducing the distance between the nanocrystals. Transmission Electron Microscopy (TEM) images show that the average distance between NCs decreases from around 2 nm with oleic acid to

0.5 nm after the ligand exchange [13]. The size of the nanocrystals is determined during the synthesis and therefore the band gap can differ between batches. For this work three batches of PbS were used: PbS 1348 ( $E_G=1.21$  eV), PbS 1522 ( $E_G=1.12$  eV) and PbS 1553 ( $E_G=1.26$  eV). Using the model of Cademartiri et al. [52], the diameters of the nanocrystals were determined. These values are listed in Table 3.1, along with the HOMO and LUMO levels which are deduced from the NC sizes using the model by Bisri et al. [53].

PbS batch	$E_G$ (eV)	NC diameter (nm)	HOMO (eV)	LUMO (eV)
PbS 1348	1.21	3.7	5.1	3.9
PbS 1522	1.12	3.9	5.1	4.0
PbS 1553	1.26	3.5	5.2	3.9

Table 3.1: The band gap, nanocrystal diameter and HOMO-LUMO levels of the different PbS batches.

### 3.7 Interlayer

In the section on tandem solar cells it was explained that the interlayer needs to meet three requirements: it has to protect the underlying layers during the solution processing, it has to act as a recombination center for electrons and holes from the subcells and it needs to be optically transparent. These requirements make the selection of the interlayer materials a crucial element in the fabrication of tandem solar cells. An issue that comes into play is that processing the interlayers from solution could result in dissolving the underlying layers, unless the solvent are orthogonal (i.e., the solvent used for the top layers cannot dissolve the materials underneath). For this reason, most of the interlayers are not processed from solution but instead vacuum deposited. Materials that can be deposited using this technique include metals and metal oxides and for this thesis only these two classes of materials have been used.

Material	Work function (eV)
Aluminum (Al)	4.3 [35]
Silver (Ag)	4.3 [54]
Tungsten oxide ( $WO_3$ )	4.8 [55]
Molybdenum oxide ( $MoO_3$ )	5.3 [56]
Zinc oxide (ZnO)	4.4 [57]
Lithium-doped zinc oxide (LZO)	4.4 [58]

Table 3.2: The interlayer materials with the work functions in eV.

The fact that the interlayer has to function as a recombination center means that the work functions of the metals or metal oxides have to be aligned to the LUMO of the front cell and to the HOMO of the back cell. The work functions of all the interlayer materials that have been used for this thesis are given in Table 3.2. It is clear that aluminum, silver zinc oxide and lithium-doped zinc oxide will be used as a cathode and that tungsten oxide and molybdenum oxide will be used as an anode in the interlayer because of the matching work function to the energy levels of the donor and acceptor materials, respectively.

Due to the third requirement of the interlayer, optical transparency, the layer should be as thin as possible to minimize the absorption of light. Typical thicknesses range from 1 nm for aluminum and silver to 45 nm for tungsten oxide. The higher thickness for the latter results from the higher transparency of the metal oxides compared to the metals [59].

### 3.8 ITO

The collection of charge carriers in a solar cell takes place at two electrodes: the anode and the cathode. The anode of the solar cells described in this thesis is a layer of indium tin oxide (ITO) on a glass substrate (3x3 cm). This is a transparent conducting oxide with a work function of 4.8 eV [35]. It is very commonly used in solar cells because of its transparency and low sheet resistance (about 13  $\Omega$ /sq) [60]. The ITO is deposited on a glass substrate. This substrate brings stability and has good optical transparency which is required since the light enters the solar cell from this side.

### 3.9 PEDOT:PSS

The hole transport layer (HTL) that was used for this thesis is poly(3,4-ethylenedioxythiophene) polystyrene sulfonate, or PEDOT:PSS. This semimetallic polymer is coated on the ITO and its function is to transport the photo-generated holes from the polymer in the active layer to the anode, while simultaneously preventing the electrons from going in the same direction. The fact that PEDOT:PSS functions as a hole transporter is clear from its work function (5.0 eV), which allows for an ohmic contact between the active layer polymer and the ITO [35]. In addition to enhancing the charge transport, the PEDOT fills up the non-uniform ITO surface, making the solar cell's layers smoother [48].

### 3.10 Cathode

The cathode of the solar cell is made of a thin layer of lithium fluoride (LiF) in combination with aluminum (Al). Since the cathode is the back contact it does not need to be transparent like the ITO. The work function of Al is 4.3 eV [35]. Bory et al. claim that adding a thin layer ( $\leq 2$  nm) of lithium fluoride to aluminum can result in lowering of the electron injection barrier of the cathode [61]. This means that the electrons can be extracted more effectively. The cathode is deposited via thermal evaporation, which is described in the next chapter.

## Chapter 4 Experimental

This chapter will describe the experimental details concerning the fabrication and testing of (tandem) solar cells. The fabrication includes the cleaning of the substrate, preparing solutions for the solution processing of the cells (spincoating) and the thermal evaporation of the metal contact. After the solar cell has gone through these steps it is ready to be tested. There are several methods that can be used for characterizing a solar cell; the most important methods are the J-V characteristics under illumination from a solar simulator and the external quantum efficiency (EQE) measurements. These methods will give a clear understanding of the solar cell's performance and allow for the direct comparison of cells in terms of power conversion efficiency. However, if there are problems with the solar cell's efficiency, these experiments can give little explanation about the source of the problems. Other methods are needed when one wants to investigate this in more detail, such as atomic force microscopy (AFM), thickness measurements or optical modeling of the solar cell. The methods that were used for this work are explained below in more detail. Every step in the preparation of the solar cells is done in a cleanroom environment to ensure that there is no contamination from dust or other unwanted particles in the devices since these particles can degrade the performance of the solar cells.

### 4.1 Cleaning substrates

As mentioned in the chapter on materials, the glass substrates have a pattern of ITO deposited on them. The ITO layer is not completely flat and has peaks sticking out which may cause shorting problems. In addition, the glass has to be cleaned to remove any dirt from its surface. For this purpose, the substrates are scrubbed with a mixture of deionized water and soap for five minutes. The scrubbing is done with textured gloves, which help in the removal of the ITO peaks. The substrates are then cleaned in an ultrasonic bath of deionized water for ten minutes, followed by an ultrasonic bath of acetone for ten minutes and an ultrasonic bath of isopropanol (ten minutes). Afterwards, the substrates have to dry in an oven at 140°C for ten minutes to remove any excess solvents. Depending on the type of solar cell, there is an additional step which involves removing any organic residues that might still be present on the substrate. This is done by treating the ITO-glass with ozone in a plasma chamber for 30 seconds. An additional effect of this treatment is that the wetting of the ITO surface changes which makes it more hydrophilic. This is beneficial for coating the PEDOT layer since this is an aqueous solution and therefore the ozone treatment is used in the case of organic and tandem solar cells. For PbS Schottky cells the ozone treatment is not used and instead the ultrasonication in acetone is done for 20 minutes to remove more organic residue.

### 4.2 Preparing solutions

The preparation of solutions for the active layer materials takes place in a nitrogen-filled glovebox. The atmosphere inside the glovebox is controlled and oxygen and water levels are reduced to <0.1 parts per million (ppm). The low O<sub>2</sub> and H<sub>2</sub>O levels are necessary since water and oxygen severely degrade the performance of the photovoltaic devices. This is also the reason why only anhydrous solvents are used for making the solutions.

The weighing of materials is done with a balance with a resolution of 0.1 mg. The material is placed directly into a vial and after weighing all the materials, the solvent is added with a micropipette for high accuracy. The vial is closed and sealed with parafilm to prevent loss of solvent through evaporation. A magnetic stirrer inside the vial is used to stir the solutions overnight on a magnetic hot plate. The temperature of the solutions while stirring varies per material and solvent, but does not exceed 90°C in this thesis. After stirring overnight, the solute should be fully dissolved. Before

the solutions are used, they are filtered to remove any undissolved solute or other particles. After filtering, the solutions are ready for the spincoating process.

### 4.3 Spincoating

The layers of the solar cell that are made via solution processing are all spincoated. This technique involves dropping a small amount of solution on the substrate, followed by fast spinning of the substrate. The centrifugal force resulting from this rotation drives the solution from the substrate, leaving a thin film behind. Important parameters in this process are the spinning speed, the acceleration of the substrate and the duration of the spinning. The first two factors determine the thickness of the layer: faster spinning leads to thinner layers. However, the concentration of the solution and the choice of solvent also influence the thickness. Therefore, it is necessary to optimize the spincoating process for each new solution. Optimization includes adjusting the speed, acceleration and duration for all stages in the process. It is common to have multiple stages in the spincoating process, each one with a different speed and/or acceleration. For example, a two-stage spincoating process can be used in which the first stage determines the thickness and the second stage is used for drying the layer by evaporating any excess solvent. The spincoater lid can be opened or closed. When the lid is closed, it is more difficult for the solvent to escape. This leads to a situation in which the environment of the substrate is filled with solvent vapor, making it harder for the solvent to evaporate from the solution. Spincoating with an opened lid is therefore mostly used in the drying stage. Some standard procedures (also called recipes) for spincoating different materials are listed in Table 4.1. These recipes also include post-coating annealing steps which can improve the layer morphology and evaporate solvent residues. It can be assumed that these recipes were used in the fabrication of all devices, unless mentioned otherwise. Apart from PEDOT:PSS, all of the materials are spincoated inside a glovebox. The exception for PEDOT:PSS stems from the fact that this layer is made from an aqueous solution.

Material	First stage				Second stage				Annealing	
	$v$ (rpm)	$a$ (rpm/s)	$t$ (s)		$v$ (rpm)	$a$ (rpm/s)	$t$ (s)		$T$ (°C)	$t$ (min)
PEDOT:PSS	500	1000	10	open	1000	1000	60	open	140	10
PbS/BDT	4000	4000	60	closed	-	-	-	-	140	1 - 5*
P3HT:PCBM	1000	1000	10	closed	1000	1000	90	open	120	5
PCPDTBT:PCBM	1200	1000	10	closed	1200	1000	90	open	120	5
P3TI:PC <sub>70</sub> BM	3300	1000	10	closed	1000	1000	110	open	140	5
ZnO/LZO	2500	2500	30	closed	1000	1000	60	open	-	-

Table 4.1: Spincoating recipes for different materials. The symbols  $v$ ,  $a$ ,  $t$  and  $T$  denote speed, acceleration, time and temperature, respectively. Open and closed refer to the position of the spincoater's lid. \* Annealing for 1 minute is used after the second and after the third coating of BDT, annealing for 5 minutes is done after finishing all the PbS and BDT layers.

The spincoating process for PbS is a little different from the polymer spincoating process. The latter only has to be coated once, whereas a lead sulfide layer consists of several spincoating steps. The reason for the layer-by-layer processing is that replacing the oleic acid ligands with BDT decreases the distance between nanocrystals. Hence, the crosslinking introduces cracks in the layer which can be filled if multiple layers of PbS are coated. The first step in the so-called layer-by-layer deposition is depositing BDT on the entire surface of the substrate and starting the spincoating process after

30 seconds, followed by spincoating a layer of PbS. This only requires depositing a small amount of the NC solution on the substrate, after which the spinning should start immediately. This is necessary because the chloroform is very volatile and the formation of the NC film starts very quickly and in an uncontrolled way. This process is repeated until the desired thickness is reached. The film is annealed at 140°C for 1 minute after the first and second layer are deposited in order to improve the adhesion to the substrate. After all the layers are deposited, the film is annealed at 140°C for 5 minutes. The total amount of PbS layers differs per tandem device because the optical modeling determines the optimal thickness for each layer. However, it is typically around 7 layers thick.

#### 4.4 Thermal evaporation

The metal cathode consisting of lithium fluoride and aluminum is deposited via thermal evaporation after all the solution-processed layers are coated. This method involves heating the material in vacuum ( $10^{-7}$  mbar) after which it evaporates and solidifies on the substrates situated above the material. The material is kept in a metallic (tungsten) boat, which is subjected to a current. The resistance of the boat causes it to heat up, melting the metal. This leads to the evaporation of the material. To ensure that the ITO contacts are not covered with the metal, which would result in a short between the anode and cathode, a mask is used to cover these areas. The rate of evaporation can be controlled by changing the current flowing through the boat, enabling an accurate determination of the thickness of the layer. The standard thicknesses of the LiF and Al layer are 1 nm and 100 nm, respectively.

Thermal evaporation is also used for the deposition of some parts of the interlayer for tandem solar cells. These materials are silver, molybdenum oxide and tungsten oxide, in addition to the already mentioned aluminum. The standard thicknesses for these layers are: 1 nm for silver, 1 nm for aluminum, 15-45 nm for tungsten oxide and 10-30 nm for molybdenum oxide. The latter two values are variable as a result of optical modeling. For the evaporation of interlayers a different mask is used. This mask covers as little as possible of the top layer of the solar cell to ensure the deposition over the biggest possible area on the cell. However, full coverage of the interlayer was not possible because the mask held the substrate in place, resulting in slight shadowing of the solar cell around the edges.

#### 4.5 Total procedure for device fabrication

The techniques that are used to make the individual layers of the solar cell are described above. The total procedure for the (tandem) cells involves spincoating a layer of PEDOT:PSS on a clean substrate outside the glovebox, after which the substrate is brought into the glovebox for the spincoating of the active layer material. In the case of a tandem solar cell with ZnO or LZO as the interlayer, this material is also spincoated (after the active layer). When all the layers are deposited, the substrate is transferred to the evaporator glovebox in a nitrogen-filled sealed container to prevent contact with oxygen. Here, the cathode layer is deposited for single cells, which are then ready to be tested. In the case of a tandem solar cell, all the remaining interlayers are evaporated. The substrate is then transported to the spincoater glovebox in the sample holder and the second active layer is coated. Afterwards, the cell is transferred to the evaporator where the cathode is deposited.

#### 4.6 J-V measurements

After the back contact has been deposited, the current density - voltage curves of the solar cells can be measured. This is done under illumination from a Steuernagel SolarConstant 1200 lamp (100 mW/cm<sup>2</sup> intensity). The spectrum of this lamp resembles that of the Air Mass 1.5 Global (AM1.5G) solar spectrum, i.e. the sun's spectrum corrected for the absorption and scattering of the light in the atmosphere. In addition, the spectrum is corrected for the non-zero solar zenith angle in middle latitude regions of the earth. The effect of this is that the path of the solar light travelling through the atmosphere is 1.5 times the atmosphere thickness. One is able to calibrate the intensity of the light to match that of the sun with a silicon reference solar cell. For this calibration, the spectral mismatch factor  $M$  is used, which is defined as follows:

$$M = \frac{\int E_R(\lambda)S_R(\lambda)\partial\lambda}{\int E_S(\lambda)S_R(\lambda)\partial\lambda} \times \frac{\int E_S(\lambda)S_T(\lambda)\partial\lambda}{\int E_R(\lambda)S_T(\lambda)\partial\lambda} \quad (4.1)$$

In this formula  $E_R$  is the AM1.5G reference spectrum and  $E_S$  is the spectrum of the solar simulator.  $S_R$  and  $S_T$  are the spectral responses of the reference cell and the tested cell, respectively. These responses are measured in the external quantum efficiency experiments which will be explained in the next section. The intensity of the solar light has to be adjusted so that the short-circuit current density of the reference cell is equal to its standard  $J_{SC}$  divided by a factor  $M$  for reliable J-V measurements.

After the light intensity has been calibrated, the J-V measurements can be carried out. All the J-V measurements are done inside a glovebox. The substrate is placed into a holder with eight contact pins. Every substrate has four solar cells with varying device areas and each solar cell has a contact for the cathode and the anode. After fabrication, the anode contact is covered by the active layers and therefore the material needs to be removed with a scalpel before putting the solar cell into place. The contact pins are connected to a Keithley 2400 SourceMeter which is used to generate a voltage over the solar cell and to measure the resulting current coming from the device. The data that the Keithley acquires are analyzed by a LabView computer program. Measuring the J-V curves is done by changing the applied voltage from 0 V to 2 V, then from 2 V to -2V and back to 0 V with steps of 0.04 V. Sweeping the voltage in this way ensures that both the forward and backward direction are scanned, which will show whether hysteresis is present in the measurement. The solar cell's active areas are confined by a metallic mask in order to define the exact areas. This prevents the illumination of other regions of the solar cell's surface which can contribute to the photocurrent. Each area of the device is measured in dark and under illumination. The temperature of the sample holder can be measured and controlled in order to keep it constant at 25°C, which is a standard condition for solar cell testing.

#### 4.7 EQE measurements

After the J-V characteristics have been measured, the samples are put into a custom made metallic sample holder, which is taken out of the glovebox for the external quantum efficiency (EQE) measurement. The sample holder is filled with nitrogen from the glovebox and it is air-tight so that the solar cell does not come in contact with oxygen. The holder also has eight contact pins for connecting the device with a Keithley 2410 SourceMeter, and a glass window for illuminating the sample.

The EQE measurement is based on the solar cell's response to monochromatic light. The EQE of a solar cell equals the amount of collected charge carriers per incident photon. This can be calculated

by measuring the generated current when the device is under illumination of monochromatic light with a known power, also called the spectral responsivity  $S_T(\lambda)$  (units:  $A W^{-1}$ ). The conversion from spectral responsivity to EQE is given in Equation 4.2. Here,  $h$  is Planck's constant,  $c$  is the speed of light,  $q$  is the elementary charge and  $\lambda$  is the wavelength of the light.

$$EQE(\lambda) = \frac{hc}{q\lambda} \times S_T(\lambda) \quad (4.2)$$

The power of incident light per unit area, or irradiance, on the solar cell can be determined from a background measurement. This is done using a photodiode (Ophir PD300 series) to measure the irradiance from the monochromatic light at a fixed distance from the source. The solar cell is placed in the same position and the power of the incident light is corrected for the solar cell's area. A Newport 6334NS Quartz Tungsten Halogen (250 Watt) lamp is used as light source. The light goes through a series of three filter wheels (a holder with multiple light filters) which ensures that the transmitted light is monochromatic. The set of filters enable transmitting light of 33 different wavelengths in the range of 1400 to 380 nm. A LabView program is used to rotate the filter wheels in order to transmit light of a different wavelength. The Keithley SourceMeter keeps the solar cell under short-circuit conditions and measures the current generated in the device when it is illuminated.

This setup can only be used to measure single cells in a reliable way, because the setup for tandem EQE measurements requires another monochromatic light source. Due to the series-connected tandem structure, the total current density through a tandem cell is determined by the lowest  $J_{SC}$  of the subcells. When monochromatic light of frequency  $\nu_1$  is used to illuminate a tandem cell in which the high band gap material has a band gap  $E_G > h\nu_1$ , only the low band gap subcell will absorb light and generate current. This makes the high band gap subcell the current-limiting cell and as a consequence no current flows through the device. Thus, the EQE spectrum would be zero at this frequency, even though photocurrent generation takes place. A solution to this issue is to excite the high band gap material with light of a higher frequency  $\nu_2$  ( $h\nu_2 > E_G$ ) to generate excess charges in that subcell [62]. Due to these excess charges, the low band gap subcell becomes the current-limiting cell and the EQE spectrum can be measured in an accurate way. The requirement is that the low band gap material has a low absorbance at the frequency  $\nu_2$  (preferably zero). Measuring the external quantum efficiency of the high band gap material can be done in a similar way.

#### 4.8 Absorbance

Absorbance measurements are carried out with a Shimadzu UV-3600 UV-Vis-NIR spectrophotometer. The absorbance  $A$  can be used to check the band gap of a material and to see the overlap in absorption spectra of materials used for tandem solar cells. The spectrophotometer measures the transmittance  $T$  of the material under investigation; the absorbance can be calculated using the relation in Equation 4.3. It is standard practice to carry out a baseline measurement of the layers that should not be included in the measurement. The measurement can then be corrected for this baseline.

$$A = -\log_{10}(T) \quad (4.3)$$

#### 4.9 Thickness measurements

It is very important to know the thicknesses of the various layers of a solar cell, especially in the case of tandem solar cells. For these measurements a Veeco Dektak 6M Stylus Profiler was used. This profilometer is in contact with a surface through its tip (stylus). This stylus can move in the vertical direction and stays in contact with the sample when it is scanned in the horizontal direction. The movements in the vertical direction are plotted as a function of the horizontal distance, which gives a surface profile. This profile can give information about the roughness of a surface. When a measurement is carried out over an incision in the layer it can give the difference in height between the top surface and the surface in the incision (the glass substrate).

#### 4.10 Light intensity measurements

The characterization of solar cells with a J-V measurement is done with a light intensity of 100 mW/cm<sup>2</sup>. This is the standard intensity used for testing in photovoltaic research since it resembles the spectrum of the sun. However, a solar cell's  $V_{oc}$ ,  $J_{sc}$ , fill factor and PCE can change drastically when the intensity of illumination is different from the standard value. The short-circuit current density of polymer solar cells increases with increasing light intensity  $I$  according to the relation  $J_{sc} \propto I^\alpha$ , with  $\alpha$  equal to 0.85 to 1 [63]. When the open-circuit voltage is plotted as a function of the light intensity in a semi-logarithmic plot (the light intensity in logarithmic scale), the slope of the line is equal to  $nkT/q$  ( $k$  is the Boltzmann constant,  $T$  is the temperature in kelvin,  $q$  is the elementary charge and  $n$  is the ideality factor) [64]. The fill factor decreases slightly when the light intensity is higher [65], which can be caused by the fact that the series resistance becomes more influential with the increased number of charge carriers at higher intensities. All of these results show that the light intensity is important for the performance of a solar cell. In the case of tandem solar cells it is also highly relevant since the back subcell is illuminated by light which first passes through the front subcell and the interlayer. Any absorption by these layers result in a reduced light intensity for the back subcell. Therefore, it is useful to characterize the performance of the individual solar cells under illumination with reduced intensity. The experiments can be carried out using a similar setup to the EQE setup. The substrate is placed in the sample holder and illuminated with the same light source, but the light does not pass through the monochromatic filters. Instead, a number of neutral density filters with different optical densities (0.1 – 1 OD) are used to reduce the intensity. The light passes through one or more of these filters and illuminates the solar cell. The cell is connected to the Keithley which sweeps through an applied voltage from 2V to -2V in steps of 0.04V, while it measures the current simultaneously. The intensity of the lamp is 100 mW/cm<sup>2</sup> without the filters and with the filters the intensity can be made lower than 1 mW/cm<sup>2</sup>.

#### 4.11 Optical simulations

The section about the theory of tandem solar cells discussed the optical spacer effect and its influence on the device performance. It demonstrates that it is crucial to optimize the thickness of each layer in the device. The optimization is done with the help of a model developed by Pettersson et al., which uses the complex index of refraction ( $\tilde{n} = \eta + i\kappa$ ) of all the materials to calculate the distribution of the optical electric field in a solar cell [37]. The complex indices of refraction are obtained with a variable angle spectroscopic ellipsometer (VASE) or from literature. The model is based on the transfer matrix formalism and assumes that all the layers are isotropic and uniform, that each absorbed photon contributes one charge to the photocurrent, and that the total current density of a tandem cell is equal to the smallest  $J_{sc}$  of the two subcells [6, 37]. The modeling is done in Matlab and involves calculating the distribution of the optical electric field through a (tandem) solar cell over a range of wavelengths (400-900 nm), while varying the thickness of the layers under investigation. It calculates the number of absorbed photons in the active layers and converts

this to a current density. Due to the assumption that all absorbed photons contribute to the photocurrent, the  $J_{sc}$  can exceed the maximum attainable value for a subcell. The model gives the distribution of the electric field within the device and a surface plot of the resulting  $J_{sc}$  as a function of the thicknesses of the layers. From this, a contour plot of the latter figure is made with a line that indicates the current matching combinations. Examples of these plots are given in Figure 5.2. The current matching conditions are used as the guidelines in the tandem fabrication.

## Chapter 5 Results

Due to the three different polymers, the three batches of lead sulfide nanocrystals and the various interlayer materials, there is a large amount of possible combinations for the tandem solar cell. In this work, the focus has been on the fabrication of five different polymer-PbS combinations. In the search for a good working tandem cell different interlayers were used. These variations each require modeling for the optimal thicknesses, which was done for most tandems. The performance of the reference solar cells is tested before they can be used in a tandem structure. The fabrication of the tandem cells and the subsequent experiments are described in this chapter. It should be noted that for each model the same batch of PbS is used.

### 5.1 P3HT:PCBM – PbS tandem

The first tandem cell that was made is the P3HT:PCBM – PbS tandem cell. Its structure was ITO/PEDOT/P3HT:PCBM/Ag/WO<sub>3</sub>/PbS/LiF/Al. The interlayer consisted of silver (1 nm) and tungsten oxide (45 nm). P3HT:PCBM was chosen for the polymer-fullerene active layer because it is a well-understood blend. In previous work a tandem with PbS as the front cell and P3HT:PCBM as the back cell was made [6], which made it straightforward to compare the device performance and to test whether this new structure performed better than the cell with the reversed structure. The location of the energy levels of the tandem cell's materials indicate that charge separation, extraction at the electrodes and recombination at the interlayer can take place (Figure 5.1).

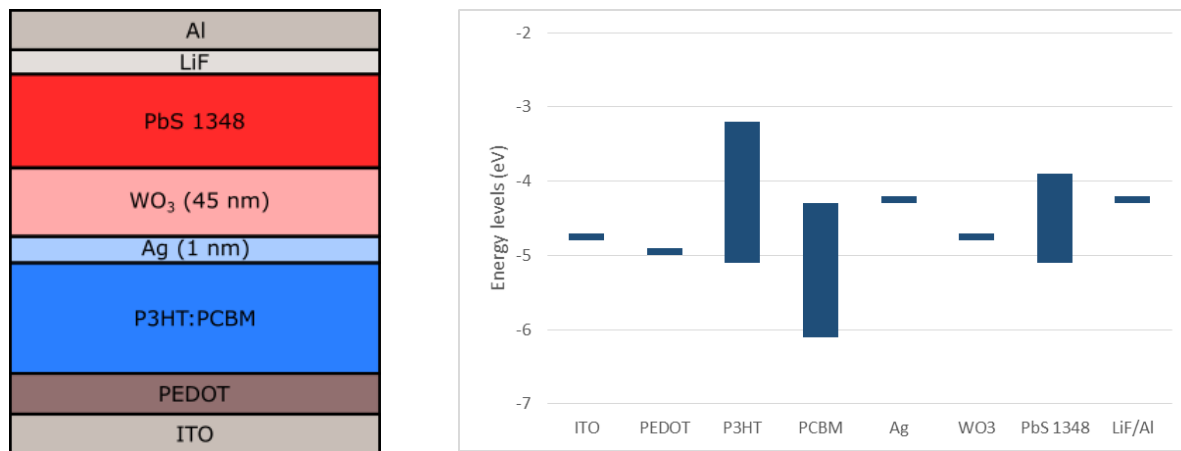


Figure 5.1: Device structure of the P3HT-PbS tandem (left). Layer thicknesses are not to scale. The energy level diagram of the tandem structure is depicted on the right.

The optical modeling was carried out with the structure depicted in Figure 5.1 (see Figure 5.2a for the distribution of the electric field in the solar cell). The contour plot in Figure 5.2b shows that the maximum current density of over 9 mA/cm<sup>2</sup> can be achieved with a thickness of 300 nm for the P3HT:PCBM layer and 230 nm for the PbS layer. In theory, all the points on the line in the contour plot in Figure 5.2b have a balanced  $J_{sc}$  for the two subcells and therefore any of these combinations of thicknesses can be used for current matching in the tandem cell. In reality, it is impossible to have a P3HT:PCBM solar cell with a  $J_{sc}$  equal to 10 mA/cm<sup>2</sup>. This is due to the fact that the layer thickness should be higher than the diffusion length of the charge carriers, leading to increased recombination. The high values for the  $J_{sc}$  (above 8 mA/cm<sup>2</sup>) are attainable, but only when the

device is fully optimized. Therefore, it is better to aim for a slightly lower short-circuit current density. Looking at the contour plot, having a thickness of 140 nm for the polymer and 100 nm for the PbS layer would result in a short-circuit current density of around 7 to 8 mA/cm<sup>2</sup>. In order to reach these thicknesses, the spincoating parameters need to be optimized. The concentration of the P3HT:PCBM solution was 15:12 mg/ml in ODCB and the concentration of PbS in chloroform was 10 mg/ml. Crosslinking of the PbS was done with a BDT solution of standard concentration (2.84 mg/ml) in acetonitrile. Seven layers of PbS were used in order to reach a thickness of 100 nm.

Three tandem solar cells were made with the configuration depicted in Figure 5.1. For each tandem cell a reference cell for the polymer-fullerene subcell was made. In this case, the structure of the polymer reference cell is ITO/PEDOT/P3HT:PCBM/LiF/Al. Here, lithium fluoride and aluminum were used for the cathode instead of silver for the ease of processing, since it allows for simultaneously evaporating the cathode for the tandem and reference cell. There is no difference in work function for silver and aluminum as evident from Table 3.2, so the replacement is justified. The reference cell is used to check the J-V characteristics of the tandem cell; it can, for example, give information about the current matching of the subcells and indicate which subcell is the current limiting element in the tandem. The reference cell is also used to determine the thickness of the active layer with the Dektak. In addition to the polymer reference cell, a PbS Schottky reference cell was made; its structure is ITO/PbS/LiF/Al. Figure 5.3 shows the absorbance of P3HT:PCBM and PbS. The two spectra have a good complementarity in the visible range (400 to 650 nm). The J-V curves of the P3HT:PCBM and PbS reference cells are shown in Figure 5.4. The values for the  $V_{OC}$ ,  $J_{SC}$ ,  $FF$  and the power conversion efficiency can be found in Table 5.1. It can be deduced from these numbers that the tandem solar cell could theoretically reach a  $V_{OC}$  of around 1V.

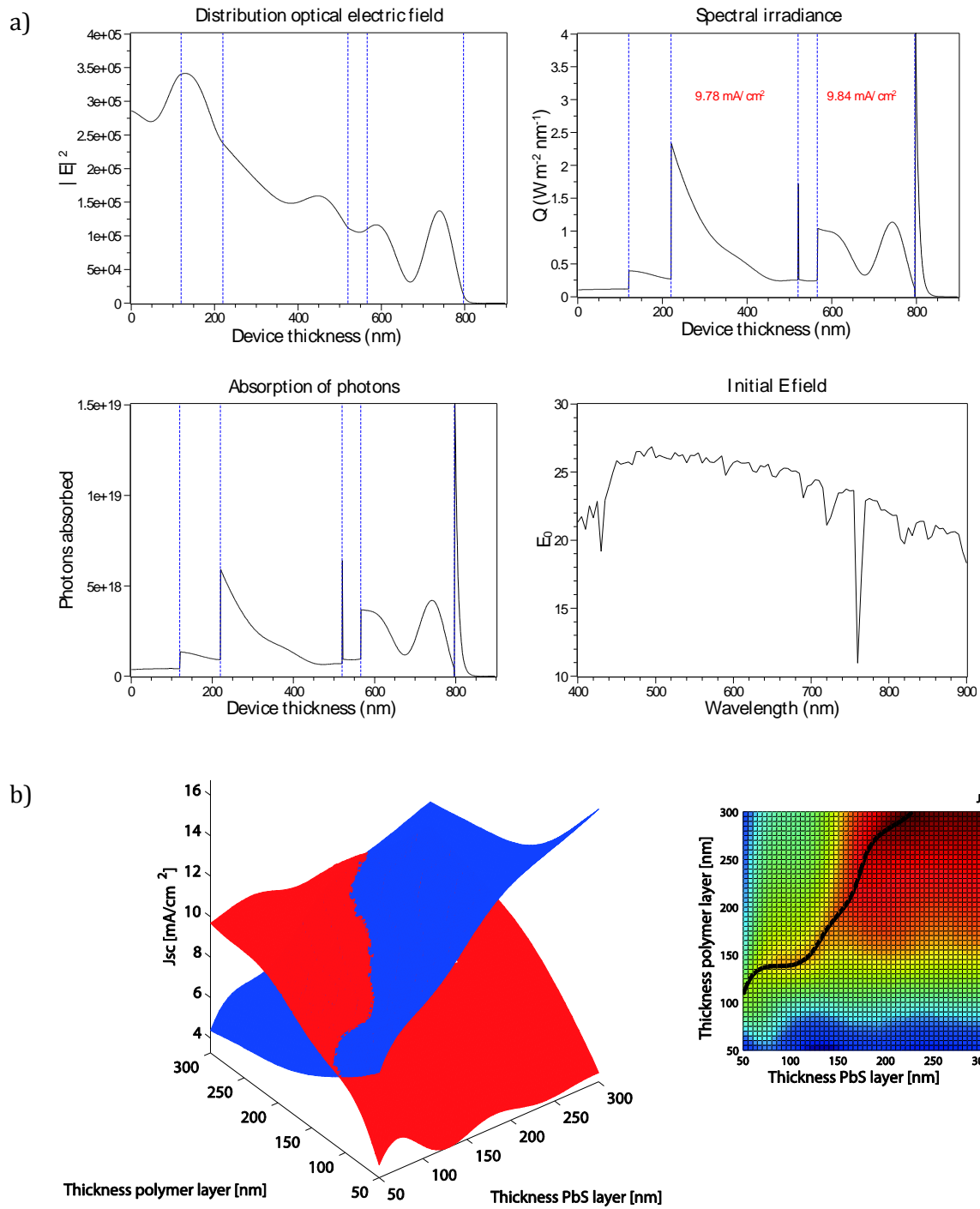


Figure 5.2: (a) A model of the distribution of the optical electric field  $E$ , along with the spectral irradiance  $Q$  and the number of absorbed photons in the solar cell. The red values in the plot for  $Q$  give the  $J_{sc}$  generated in the subcells in mA/cm<sup>2</sup>.  $E_0$  is the initial field. (b) A surface plot of the short-circuit current density for each thickness in the subcells. The intersection of the two surfaces indicate a balance in the short-circuit currents of the subcells. The intersection is depicted in the contour plot on the right for clarity. Here, the black line indicates the intersection of the two surfaces. The color bar gives the value for the  $J_{sc}$ .

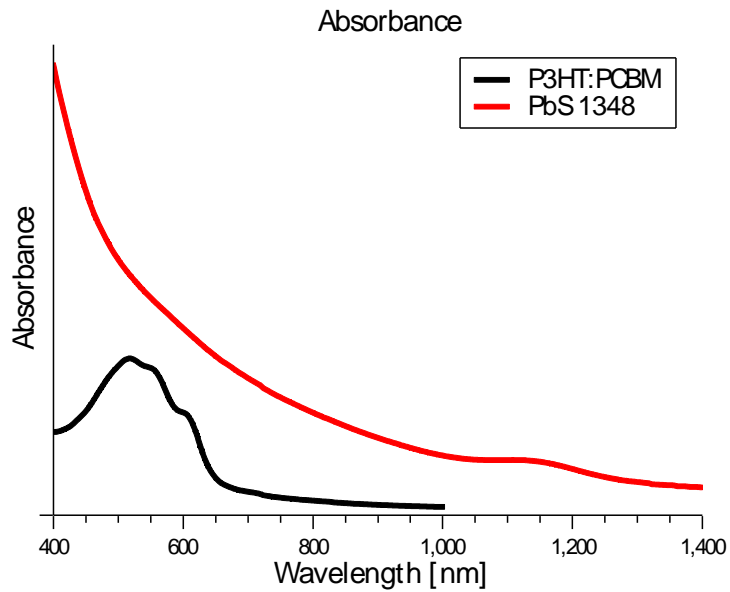


Figure 5.3: The absorbance spectra of PbS and P3HT:PCBM.

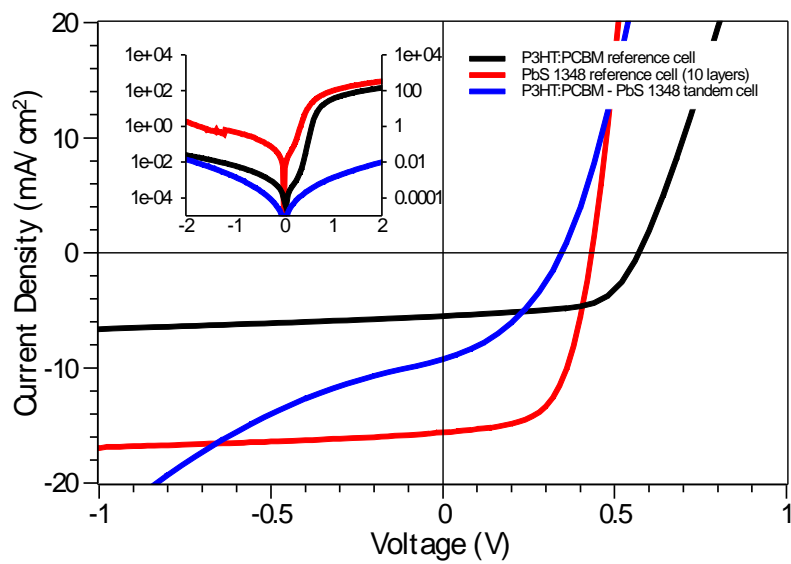


Figure 5.4: Current density - voltage ( $J$ - $V$ ) plots of the P3HT:PCBM - PbS tandem cell and the reference cells. The curves in the inset are the  $J$ - $V$  curves of the solar cells in the dark. It should be noted that ten layers of PbS were used for the reference, whereas only eight layers of PbS were used in the tandem cell. This means that the  $J_{sc}$  here is slightly higher than the value in the tandem configuration.

Device	$V_{oc}$ (V)	$J_{sc}$ (mA/cm <sup>2</sup> )	FF	PCE (%)
P3HT:PCBM	0.570	5.5	0.61	1.91
PbS	0.432	15.6	0.60	4.02
P3HT – PbS tandem	0.40	10.5	0.42	1.76

Table 5.1: J-V characteristics of the P3HT – PbS tandem cell and the subcells.

In the first experiment on this structure the P3HT:PCBM layer was spincoated according to the standard recipe, with the speed in the first stage modified to 2200 rpm. This led to a thickness of about 125 nm for the polymer layer and this is slightly too thin according to the simulation. In addition, the front subcell was damaged by the solvent of the lead sulfide nanocrystals, and as a result only two out of four areas on the device worked. The J-V characteristics (Table 5.1) reveal that the  $J_{sc}$  equals 10.5 mA/cm<sup>2</sup>, a value that is unattainable for P3HT:PCBM solar cells. This means that the solar cell did not work as a series-connected tandem cell. All of the values indicate that the photovoltaic performance of this solar cell is mostly due to the nanocrystals. Another problem was that the polymer layer was very rough, probably due to the high spincoating speed. Follow-up experiments focused on decreasing the roughness of the P3HT:PCBM layer and, more importantly, to coat the lead sulfide layer without destroying the underlying layers.

In both experiments the spincoating speed of P3HT in the first stage was set to 1500 rpm. The resulting thickness was measured to be 60 nm, which is very thin and not optimal for the tandem. As in the first experiment, the underlying layers were damaged when the spincoating of the PbS NCs took place. In the third experiment the process of degradation was clearly visible. The layers (polymer layer and interlayer) started to show scratches, gaps or other areas where the material seemed to be removed after spincoating a few (1-2) layers of lead sulfide. It was unclear whether the removed material was the active layer of the front subcell, the interlayer, or both. Neither of the tandem devices was finished and hence no J-V curves are available. Since the P3HT:PCBM - PbS tandem cell is not the optimum device structure due to the poor match of the absorbance spectra of both active layers, it was decided to progress to another polymer (PCPDTBT) and to try to solve the problem with the tandem fabrication for this configuration.

## 5.2 PCPDTBT:PCBM – PbS tandem

The structure of this tandem cell is ITO/PEDOT/PCPDTBT:PCBM/Al/WO<sub>3</sub>/PbS/LiF/Al. This structure and its energy levels are displayed in Figure 5.5. Absorbance plots of the polymer-fullerene layer PCPDTBT:PCBM and PbS NCs show that this polymer is a better option for the tandem cell configuration than P3HT because it has less overlap with the absorbance spectrum of the nanocrystals (see Figure 5.6). The interlayer was changed with respect to the P3HT tandem; the silver cathode was replaced by aluminum (1 nm) and the thickness of the tungsten oxide layer was reduced from 45 to 15 nm. The cathode material was replaced because there was uncertainty whether the 1 nm thick silver layer was uniform or had holes in it. Decreasing the thickness of the tungsten oxide layer was done for better light transmission to the back cell.

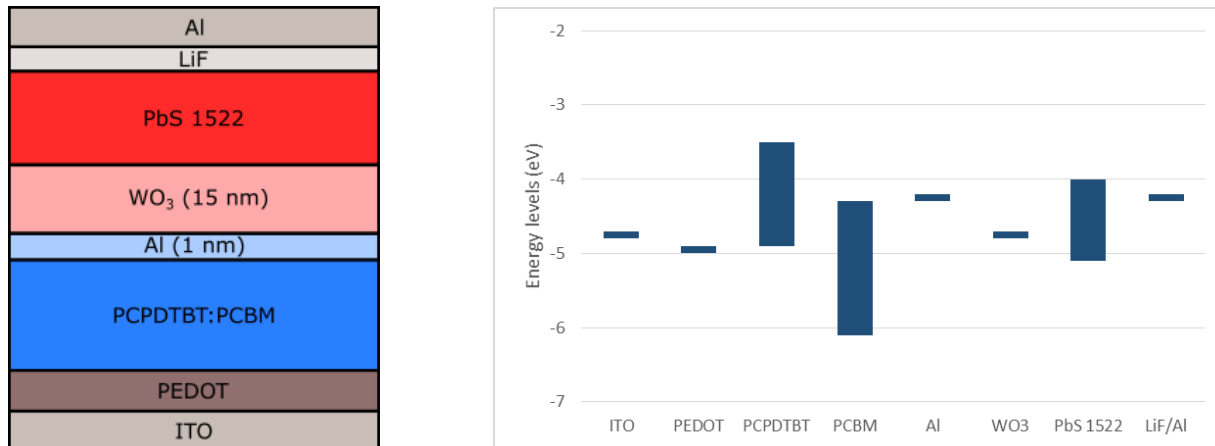


Figure 5.5: The device structure of the PCPDTBT:PCBM – PbS tandem (left) and the energy levels of the constituent materials (right).

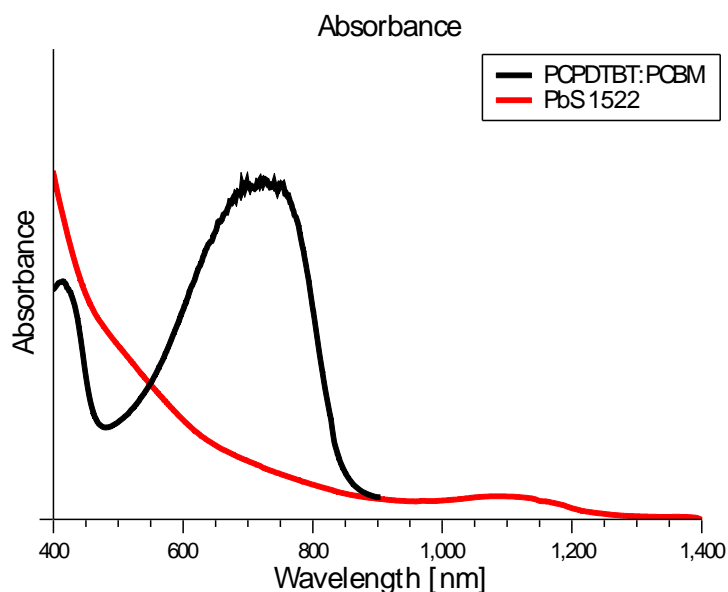
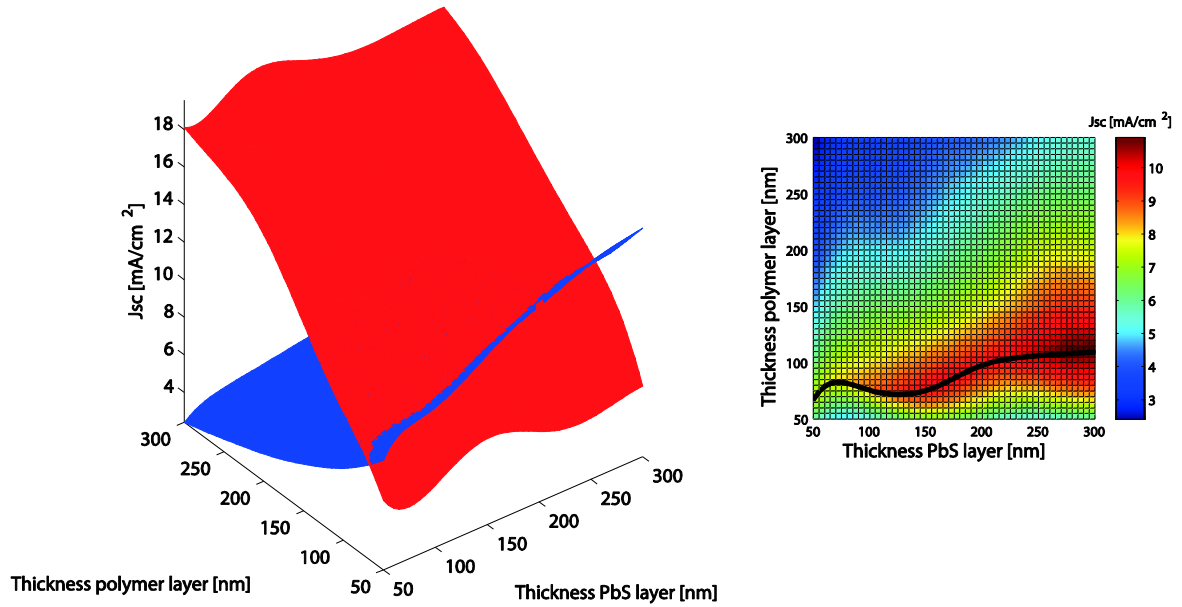


Figure 5.6: Absorbance spectra of PbS and PCPDTBT:PCBM films. The latter was made with a solution with a mass ratio of 1:1.

Optical modeling was carried out for determination of the optimal thicknesses for the active layers. The results are given in Figure 5.7a. Data on the complex index of refraction for PCPDTBT:PCBM in a 1:2 mass ratio was not available. Instead, the  $\tilde{n}$ -values for a ratio of 1:3 were used. It is assumed that the difference for the model is negligible because the absorption of PCBM becomes significant around 400 nm [50] and the model only takes wavelengths higher than 400 nm into account. From Figure 5.7a the optimal thicknesses for the PCPDTBT:PCBM and PbS layers are determined to be 75 nm and 125 nm, respectively. This would result in a tandem with a  $J_{sc}$  of 7-8 mA/cm<sup>2</sup>.

a)



b)

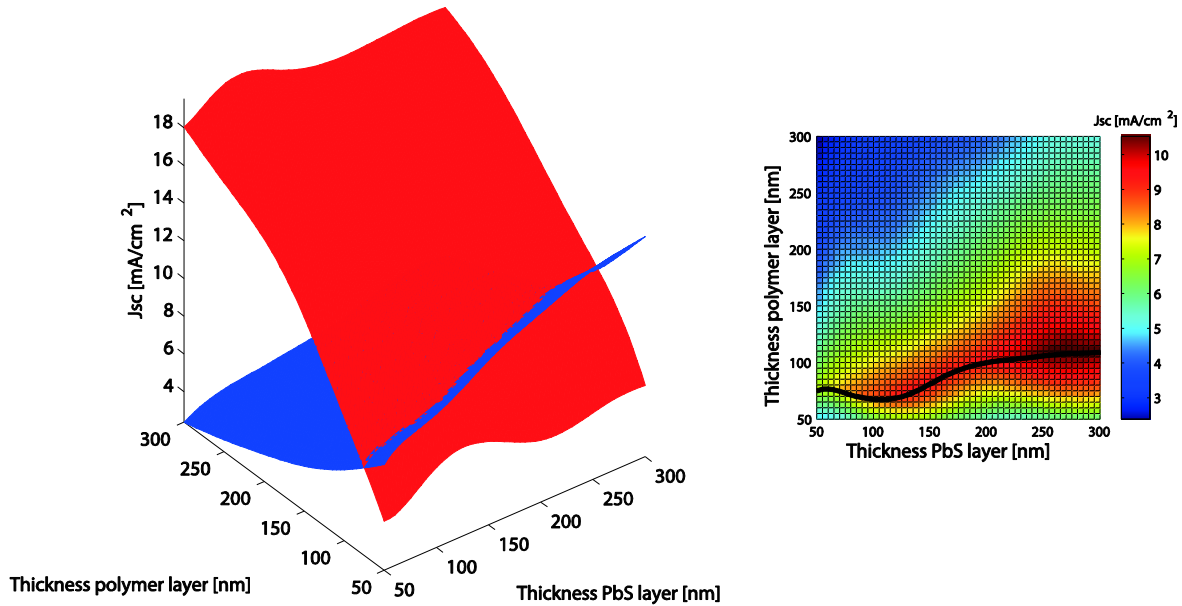


Figure 5.7: Optical simulations for the short-circuit current density as a function of the active layer thicknesses of the PCPDTBT:PCBM – PbS tandem cell. The thickness of the tungsten oxide interlayer is 15 nm in (a) and 45 nm in (b).

Reference cells for the PCPDTBT:PCBM layer were made from a solution with 17.5:35 mg PCPDTBT:PCBM per ml chlorobenzene, with the additive ODT (43  $\mu$ l/ml) for better layer morphology. The resulting solar cell, with the structure ITO/PEDOT/PCPDTBT:PCBM/LiF/Al, had a power conversion efficiency of 1.23%. Its J-V curve is plotted in Figure 5.8. It was found that the thickness of the PCPDTBT:PCBM layer fluctuated significantly across the substrate (up to 50 nm difference). This made it challenging to reproduce layers. Figure 5.8 also shows the J-V curve of a PbS reference cell. It should be noted that this device was not made for this experiment and is only displayed for an indication of the photovoltaic performance of the PbS subcell. The thickness of the cell (160 nm) was higher than the ideal value according to the optical simulations (125 nm). Therefore, the  $J_{sc}$  is overestimated in this case. The parameters of both cells are listed in Table 5.2.

The maximum attainable  $V_{oc}$  of the tandem solar is 1.1 V, according to the sum of the open-circuit voltages of both reference cells. It is clear that the PCPDTBT reference cell is the current-limiting cell, and the value for the  $J_{sc}$  is lower than the calculated value in the simulation. This is the result of a high series resistance, in combination with a low shunt resistance. The former is evident from the slope of the curve at  $V > V_{oc}$ ; the slope is more flat than the ideal solar cell's J-V curve. The low shunt resistance is indicated by the slope of the reverse current. Ideally, the slope should be flat under reverse bias (as for the P3TI reference cell) as a result of the ideal diode equation (Equation 2.2).

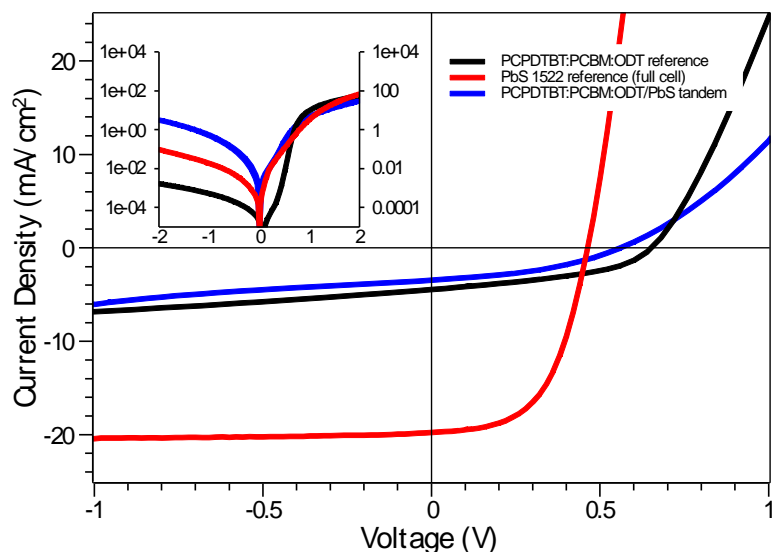


Figure 5.8: J-V curves of the PCPDTBT:PCBM - PbS tandem described in Figure 5.5, the PCPDTBT:PCBM reference cell and a PbS device. The red curve displays the J-V behavior of a full PbS solar cell, with a thickness of around 160 nm. This active layer is too thick for the tandem structure and the PbS reference here was not made for this experiment. This means that the current density is overestimated with respect to the PbS subcell of the tandem, and hence, the curve is only used as an approximation for a PbS reference cell with the ideal thickness of 125 nm.

According to Figure 5.7a, the desired thicknesses for the PCPDTBT:PCBM tandem were 125 nm for the PbS subcell and 80 nm for the polymer subcell. As for the P3HT - PbS tandems, it was damaged after spincoating all the lead sulfide layers. However, the damage was limited in this case and this enabled measuring the J-V curves of the cell (see Figure 5.8). The  $V_{oc}$  of the tandem cell is lower (0.56 V) than that of the PCPDTBT:PCBM reference cell (0.65 V). Moreover, the  $J_{sc}$  (3.45 mA/cm<sup>2</sup>) and fill factor (0.39) are low. The polymer reference cell is not optimized and, as a result, this cell is limiting the PCE of the tandem. It was mentioned above that the thickness of the polymer layer fluctuated and in this case the thickness reached a value of 140 nm, whereas previously the same spincoating program for PCPDTBT:PC<sub>70</sub>BM resulted in a layer with a thickness of about 80 nm. However, this layer also suffered from a high roughness and the thickness was not constant throughout the entire sample.

Device	$V_{oc}$ (V)	$J_{sc}$ (mA/cm <sup>2</sup> )	FF	PCE (%)
PCPDTBT:PCBM reference	0.651	4.44	0.42	1.23
PbS reference	0.463	19.75	0.55	5.02
PCPDTBT - PbS tandem	0.560	3.45	0.39	0.75

Table 5.2: Photovoltaic parameters of the devices displayed in Figure 5.8.

For the next tandem, the thickness of the tungsten oxide layer was increased to 45 nm. Figure 5.7b shows the calculated  $J_{SC}$  for the new device structure. It is clear that the thicker  $WO_3$  layer has little influence on the optimal thicknesses for the subcells. The spincoating speed for the PCPDTBT layer was changed from 1200 to 1400 rpm to prevent the polymer layer from getting too thick. However, the measures did not have the desired effect: the coating of PbS resulted in a reduced thickness in the active areas of the solar cell because of the dissolution of underlying layers by the chloroform in the PbS solution. The device was not finished due to the damage to the cell. The poor photovoltaic performance and reproducibility of the PCPDTBT:PCBM based solar cells led to the discontinuation of the use of this polymer. Poly[N,N'-bis(2-hexyldecyl)isoindigo-6,6'-diyl-alt-thiophene-2,5-diyl] (P3TI) was used as its replacement in the tandem cell structure.

### 5.3 P3TI:PC<sub>70</sub>BM – PbS tandem

P3TI, with its band gap of 1.5 eV, is an excellent material for a polymer-PbS tandem cell (see the absorbance plots in Figure 5.9). It is used in a blend with the PC<sub>70</sub>BM fullerene, leading to solar cells with open-circuit voltages up to 0.74 V. Combining this with the 0.45 V of PbS could result in a tandem cell with a total  $V_{OC}$  of about 1.2 V. The first tandem structure with this polymer was ITO/PEDOT/P3TI:PC<sub>70</sub>BM/Al/ $WO_3$ /PbS/LiF/Al (see Figure 5.10). From the energy level diagram it is clear that the chosen materials are suitable for efficient photovoltaic operation. The thicknesses of the interlayer were 1 nm (Al) and 45 nm ( $WO_3$ ). Optical simulations could not be carried out because data on the complex index of refraction of the polymer-fullerene blend was not available. There were no standard recipes for this material due to a lack of experience with P3TI. Therefore, the optimization had to be done by experimenting with the spincoating program of the polymer and investigating its influence on the overall device performance.

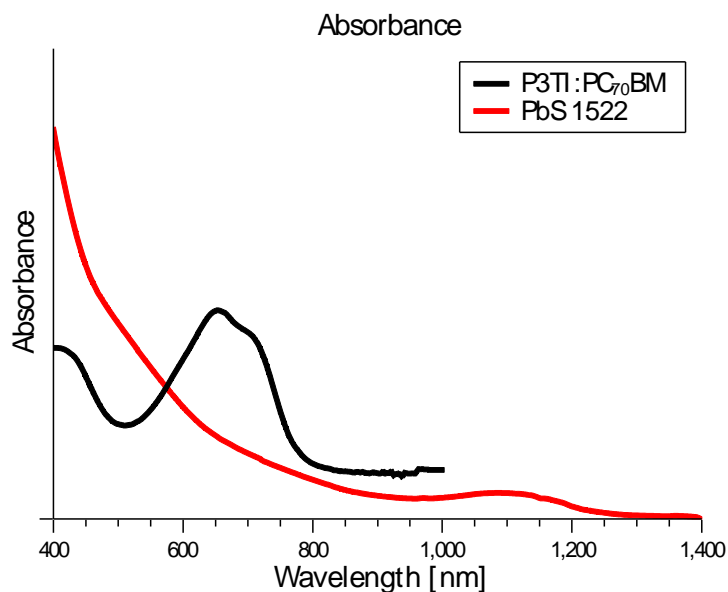


Figure 5.9: Absorbance of PbS and P3TI:PC<sub>70</sub>BM. The absorbance of both materials shows good complementarity between 400 and 800 nm.

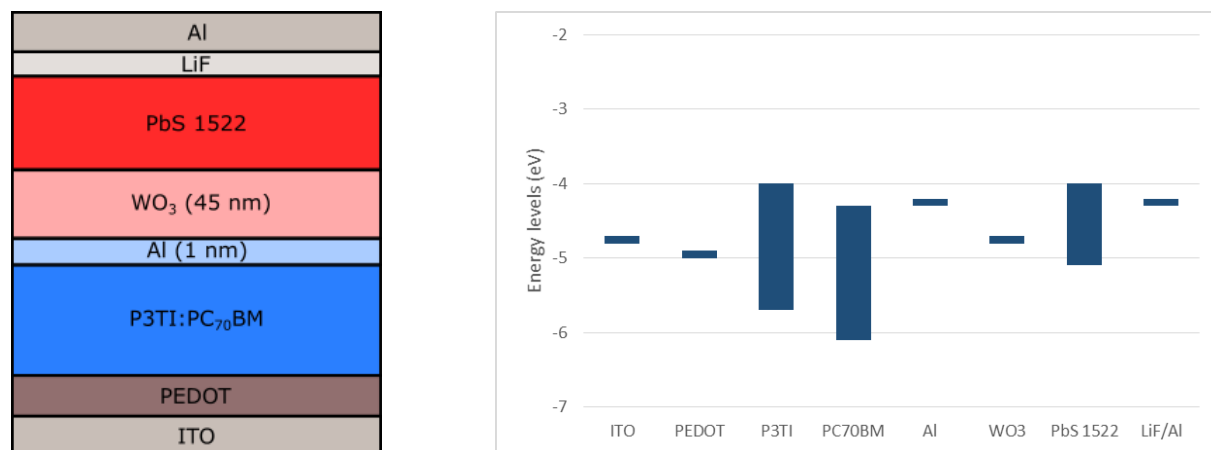


Figure 5.10: Schematic illustration of the P3TI:PC<sub>70</sub>BM – PbS device structure (left). The energy levels of the layers are plotted in an energy level diagram on the right.

P3TI:PC<sub>70</sub>BM (20:30 mg/ml) in ODCB with 2.5% (v/v) DIO was used as the solution for the polymer subcell. The P3TI layer was spincoated at 3000 rpm instead of the speed mentioned in Table 4.1. The J-V curves of the reference cell are plotted in Figure 5.11. A comparison between an annealed (5 minutes at 140°C) and a non-annealed sample was made and it was found that annealing enhances the device performance significantly (see Table 5.3). As a result, the annealing was included in the standard spincoating procedure for P3TI. For the back subcell of the tandem eight layers of PbS NCs were coated. After spincoating these layers, there was damage to the tandem cell around the active areas. However, thickness measurements of the layers indicated that there was still a significant amount of both materials present in the cell. The tandem cell had a  $V_{OC}$  equal to 0.793 V, which is greater than the open-circuit voltages of the two subcells. This means that there

was a series connection between the two subcells through the interlayer. However, the tandem cell did not work properly due to a very low  $J_{sc}$  (around 1 mA/cm<sup>2</sup>) (Figure 5.11). This could be explained by the damage to the cell in combination with a high series resistance in the device. It was assumed that this high series resistance was caused by the thickness of the interlayer and the P3TI layer (120-155 nm). Therefore, the next experiment focused on reducing this unwanted resistance by decreasing both the thickness of the P3TI layer and of the WO<sub>3</sub> layer.

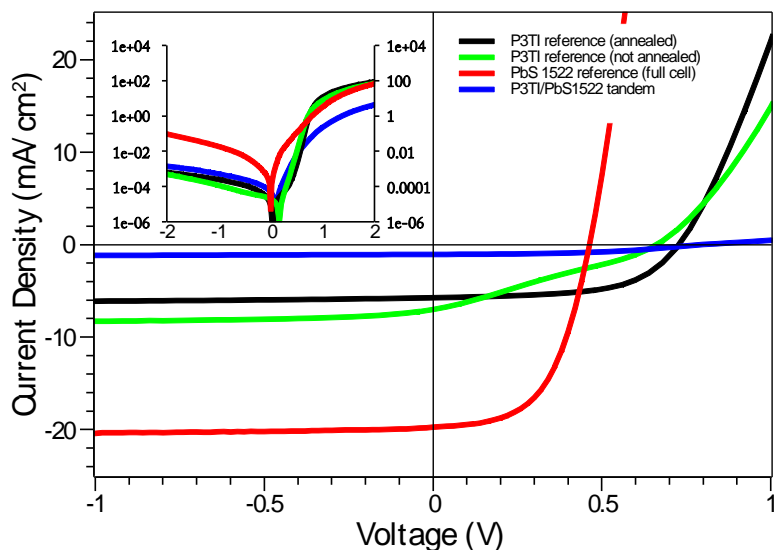


Figure 5.11: J-V curves of the P3TI-PbS tandem cell (1 nm Al and 45 nm WO<sub>3</sub> interlayer), P3TI reference cells and PbS reference cell. The P3TI:PC<sub>70</sub>BM reference cells are annealed (black curve) or not annealed (green curve). The PbS reference cell is the same as in Figure 5.8 and is included as an indication of the photovoltaic performance of the PbS subcell.

Device	$V_{oc}$ (V)	$J_{sc}$ (mA/cm <sup>2</sup> )	FF	PCE(%)
P3TI:PC <sub>70</sub> BM (not annealed)	0.661	7.0	0.26	1.22
P3TI:PC <sub>70</sub> BM (annealed)	0.727	5.7	0.58	2.43
PbS reference	0.463	19.75	0.55	5.02
P3TI – PbS tandem	0.793	1.1	0.47	0.39

Table 5.3: The J-V characteristics of the P3TI:PC<sub>70</sub>BM and PbS reference cells and the P3TI – PbS tandem.

For the second tandem the P3TI spincoating recipe was changed to that mentioned in Table 4.1 and a 15 nm WO<sub>3</sub> layer was used as the interlayer anode. The former measure led to an active layer thickness of around 110-120 nm. The tandem cell could not be improved because it was damaged during the processing of PbS layers (see Figure 5.12). Its J-V characteristics are given in Table 5.4. The value of the  $V_{oc}$  (0.83 V) is higher than the open-circuit voltages of the subcells (0.73 and 0.46 V for the front and back cell), which indicates that the device behaves as a tandem. However, the increase in  $V_{oc}$  with respect to that of the P3TI cell is very small. The lack of good results for the tandem experiments indicated that there was a flaw in the structure of the devices. It was assumed that the interlayer materials did not protect the underlying layers during the PbS spincoating process, and subsequent experiments focused on replacing the interlayer materials to materials that offer more protection.

Device	$V_{oc}$ (V)	$J_{sc}$ (mA/cm <sup>2</sup> )	FF	PCE(%)
P3TI:PC <sub>70</sub> BM reference	0.733	7.0	0.67	3.42
P3TI – PbS tandem (15 nm WO <sub>3</sub> )	0.832	1.1	0.40	0.38

Table 5.4: Comparison between the J-V characteristics of the P3TI-PbS tandem cell (with a 15 nm WO<sub>3</sub> interlayer) and the polymer reference cell.

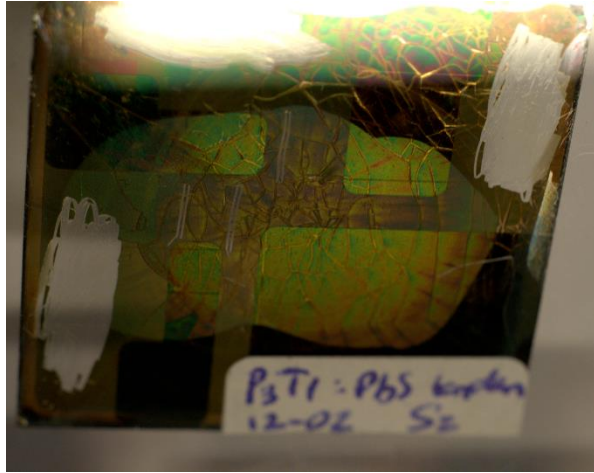


Figure 5.12: Photograph of the P3TI:PC<sub>70</sub>BM – PbS tandem solar cell with the 15 nm WO<sub>3</sub> interlayer. There is a lighter area around the metal electrodes of the device where material was removed during the spincoating of lead sulfide. Additional damage in the form of cracks in the active layer is also visible. The vertical double scratches and the areas on the edges where all material is removed are made for the thickness measurements and J-V characterization, respectively.

#### 5.4 P3TI:PC<sub>70</sub>BM – PbS tandem with LZO interlayer

Until this experiment, aluminum was used as the cathode material in the interlayers of the tandems. Replacing the Al layer by a different material with a higher transmittance allows the use of a thicker layer. If this thicker layer is free of holes, this could ensure that the front subcell remains intact during the solution-processing of the back subcell. An excellent candidate for the replacement of aluminum as the interlayer cathode is lithium-doped zinc oxide. The work functions of the materials are nearly identical, as evident from Table 3.2. The lithium-doped zinc oxide layer is solution-processable; the material comes in the form of nanoparticles dissolved in butanol. The solution had to be sonicated for 2 hours before it could be used in the spincoating process to prevent the agglomeration of the nanoparticles. The LZO layers were spincoated according to the recipe mentioned in Table 4.1, which resulted in a 20 nm thickness. The interlayer was completed by evaporating 15 nm of WO<sub>3</sub>. The total tandem structure was ITO/PEDOT/P3TI:PC<sub>70</sub>BM/LZO/WO<sub>3</sub>/PbS/LiF/Al, this structure is shown Figure 5.13.

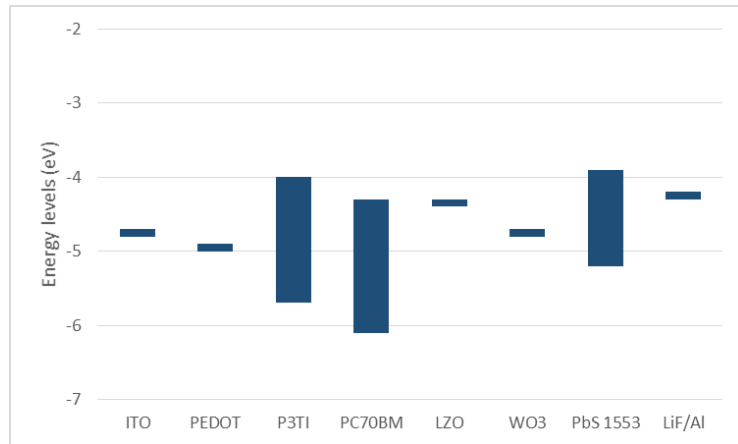


Figure 5.13: The device structure of the P3TI – PbS tandem with LZO and WO<sub>3</sub> as the interlayer materials. The energy levels of the layers are depicted on the right.

Before LZO was used in a tandem structure, it was first tested in a P3TI reference cell. The structure of this cell was ITO/PEDOT/P3TI:PC<sub>70</sub>BM/LZO/Al. Here, the LZO layer replaced the LiF which is normally used in the reference cells. Its performance was compared to a cell with the standard LiF/Al cathode. The J-V curves of both cells (Figure 5.14) indicate that the device with LZO functions almost as good as the standard cell. There is a slight difference in the short-circuit current densities and fill factor but the  $V_{OC}$  is identical for the two cells (see Table 5.5). This result demonstrated that the LZO layer could be used as an electron transport layer in a solar cell with P3TI:PC<sub>70</sub>BM as the active layer.

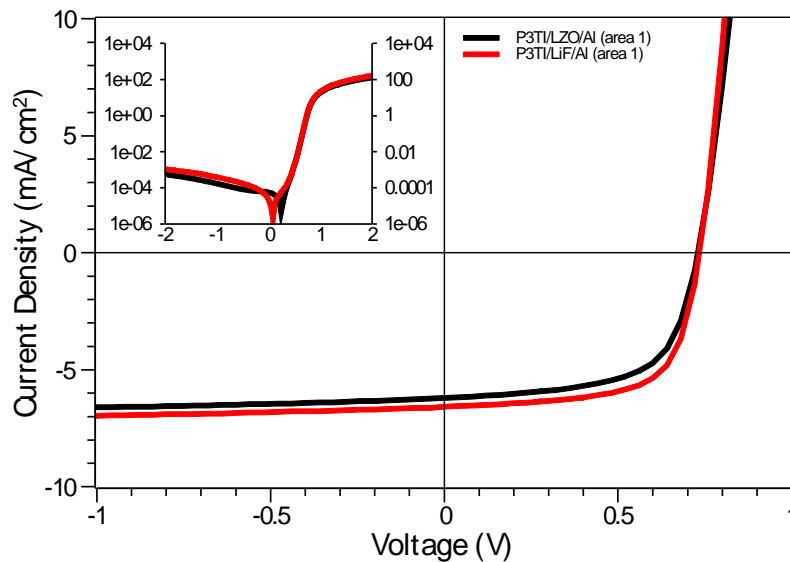


Figure 5.14: Current density – voltage plot of P3TI:PC<sub>70</sub>BM solar cells with a cathode made of LZO/Al or LiF/Al.

Cathode	$V_{oc}$ (V)	$J_{sc}$ (mA/cm <sup>2</sup> )	FF	PCE (%)
LZO/Al	0.734	6.8	0.61	3.05
LiF/Al	0.733	7.0	0.67	3.42

Table 5.5: J-V characteristics of P3TI:PC<sub>70</sub>BM solar cells with different cathodes.

The nanocrystal layer of the P3TI:PC<sub>70</sub>BM – PbS tandem was made by spincoating eight layers of the chloroform-based PbS solution (10 mg/ml). A PbS reference cell with the same amount of layers was also made. The structure of this cell was ITO/WO<sub>3</sub>/PbS/LiF/Al; the tungsten oxide layer (15 nm) was included to match the structure of the PbS subcell of the tandem. Despite the new interlayer structure, the tandem cell was damaged during device processing. The top layer of the cell had cracks similar to those visible in Figure 5.12. As a result, the photovoltaic performance of the device was poor. The J-V curves of the tandem and reference cells are given in Figure 5.15. The parameters of the curves are summarized in Table 5.6. It is apparent that, despite the damage to the active layers, the tandem cell has a higher  $V_{oc}$  than the subcells, reaching 81% of the sum of the  $V_{oc}$ s of the subcells. However, the current density is very low and limits the PCE severely. Another fact that can be concluded from the J-V curves is that the shunt resistance of the PbS reference cell is low. It is possible that this is caused by the additional tungsten oxide layer because previous reference cells without WO<sub>3</sub> showed much better behavior under reverse bias (see Figure 5.4). If this is the case, then replacing the tungsten oxide layer by a different anode material could improve the PCE of the tandem device. Further research on this will be described later.

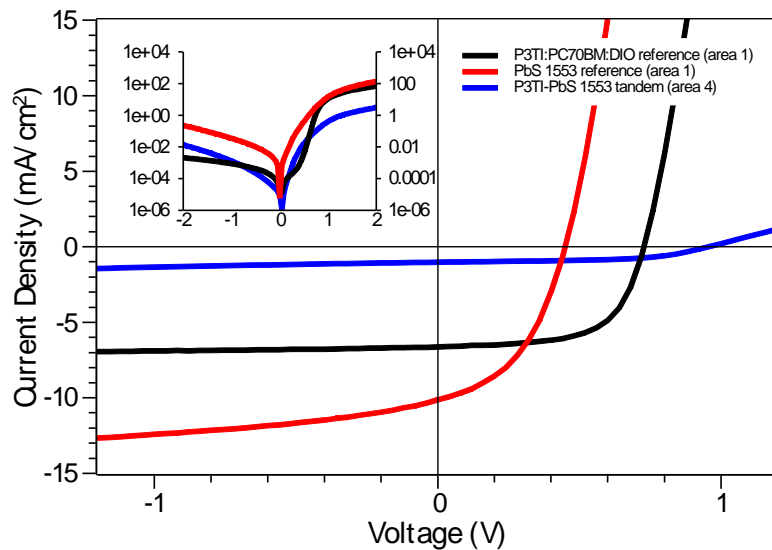


Figure 5.15: J-V curves of the P3TI:PC<sub>70</sub>BM/LZO/WO<sub>3</sub>/PbS tandem solar cell and the corresponding reference cells.

Device	$V_{oc}$ (V)	$J_{sc}$ (mA/cm <sup>2</sup> )	FF	PCE (%)
P3TI:PC <sub>70</sub> BM reference	0.727	6.6	0.62	3.00
PbS reference	0.449	10.1	0.44	2.02
P3TI – PbS tandem	0.954	1.0	0.55	0.53

Table 5.6: *J-V characteristics of the solar cells plotted in Figure 5.15.*

The previous experiments with the polymer – lead sulfide tandem solar cell demonstrated that the major challenge was to coat the lead sulfide without destroying the underlying layers. When this is realized, further optimization of the tandem structure can take place. It was important to find out what enabled the dissolution of the underlying layers by chloroform. For these experiments P3HT:PCBM was chosen as the active layer in the front subcell of the tandem.

### 5.5 P3HT:PCBM – PbS tandem with ZnO interlayer

Replacing the interlayer materials in previous experiments did not result in undamaged tandem solar cells. The possibility exists that the interlayer was not causing the problems with the tandem fabrication. It was hypothesized that the chloroform in the lead sulfide solution infiltrated the layers underneath the interlayer at the edges of the device. In the section on thermal evaporation it was mentioned that the masks used for the interlayer deposition overlap with the substrate. This made it impossible to evaporate the interlayer materials across the entire substrate; the edges were devoid of interlayer materials (this is also visible around the edges of the device in Figure 5.12). A new mask was designed for the interlayer evaporation, which increased the surface coverage of the interlayer materials. This mask was used for all subsequent tandem cells.

The previous interlayer structure was used in combination with a P3HT:PCBM front subcell to see whether the new measure had effect. However, the LZO was changed to ZnO. This material has the same work function and follows the same spincoating procedure as LZO. A comparison between ZnO, LZO and LiF as a part of the solar cell's cathode has been made and demonstrated that there is no difference between ZnO and LZO and only little difference between ZnO and LiF in terms of device efficiency (Figure 5.16). This enabled the use of ZnO in the tandem structure. An additional change was the increase of the WO<sub>3</sub> layer thickness from 15 to 30 nm to ensure good coverage of this material.

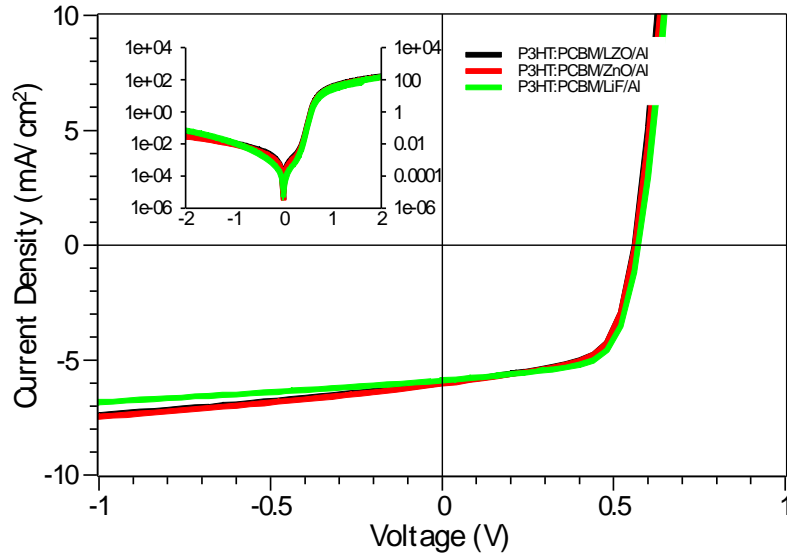


Figure 5.16: Comparison of the J-V curves of P3HT:PCBM solar cells with different cathode materials.

Optical simulations of the ITO/PEDOT/P3HT:PCBM/ZnO/WO<sub>3</sub>/PbS/LiF/Al tandem were carried out. The thicknesses of ZnO and WO<sub>3</sub> were set to 20 and 30 nm. Figure 5.17 shows the  $J_{sc}$  as a function of the active layer thicknesses. Practical values for the ideal thicknesses were determined to be about 125 nm for the polymer subcell and 100 nm for the nanocrystal subcell. This would result in a  $J_{sc}$  of 7 to 8 mA/cm<sup>2</sup>. To achieve these thicknesses, the P3HT:PCBM solution (20:16 mg/ml in ODCB) was spincoated according to the standard recipe. The back subcell was made by spincoating seven layers of nanocrystal solution (10 mg/ml in chloroform). Dektak measurements confirmed that the thicknesses were in close agreement with the desired values; the P3HT layer was 120 nm thick and the PbS layer had a thickness of around 110 nm.

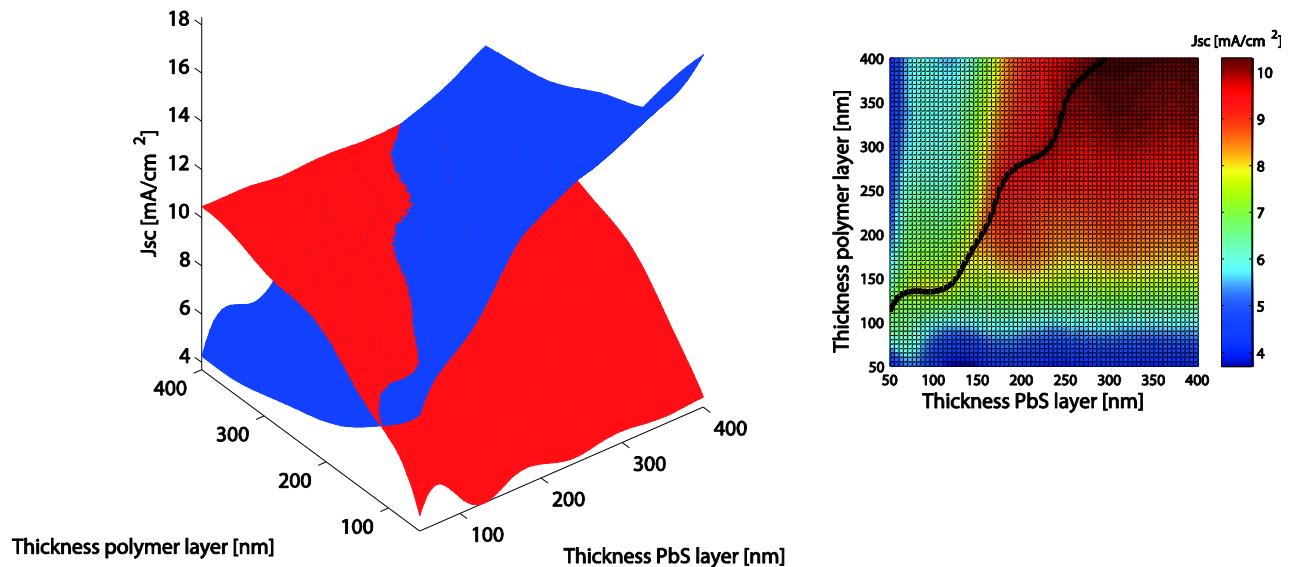


Figure 5.17: Optical simulations for the ITO/PEDOT/P3HT:PCBM/ZnO/WO<sub>3</sub>/PbS/LiF/Al tandem. The thickness of the WO<sub>3</sub> layer is 30 nm.

The coating of PbS led to a damaged film again, as for the previous tandems. However, the performance of this tandem was much better than its predecessors, as can be seen in Figure 5.18. The  $V_{oc}$  of the tandem was 0.747 V, which is 74% of the sum of the open-circuit voltages of the subcells (Table 5.7). The parameters listed in this table also show that the power conversion efficiency of the tandem cell (1.64%) is higher than that of the polymer reference cell (1.26%), and almost identical to the PCE of the lead sulfide cell (1.65%). It is remarkable that the  $J_{sc}$  of the tandem cell exceeds that of the polymer subcell, as Equation 2.7 dictates that the subcell with the lowest short-circuit current density is the current limiting cell. There are two possible explanations for this behavior. The first one concerns the mismatch factor of the tandem cell. It was mentioned in the EQE section that it was not possible to measure the external quantum efficiency of a tandem cell in a reliable way with the available setup. This means that there was no data to calculate the mismatch factor of tandem cells, hence, the appropriate intensity for measuring accurate J-V curves was unknown. It was decided to set the intensity equal to that used for the lead sulfide cells. This is sensible in view of the light intensity that reaches the back subcell, but a side effect is that the front cell will receive light of a higher intensity than the AM1.5G equivalent. This can lead to a slight overestimation of the  $J_{sc}$  of the tandem because the current-limiting front cell is generating more current than the reference cell. The second explanation is that the interlayer materials are different from the cathode materials in the polymer reference cell. The optical spacer effect could play a role here, by changing the distribution of the optical electric field in a way that is more favorable for the tandem cell. Disregarding the possible overestimation of the current density, it is remarkable that a damaged cell can still reach a  $J_{sc}$  of 5.1 mA/cm<sup>2</sup>.

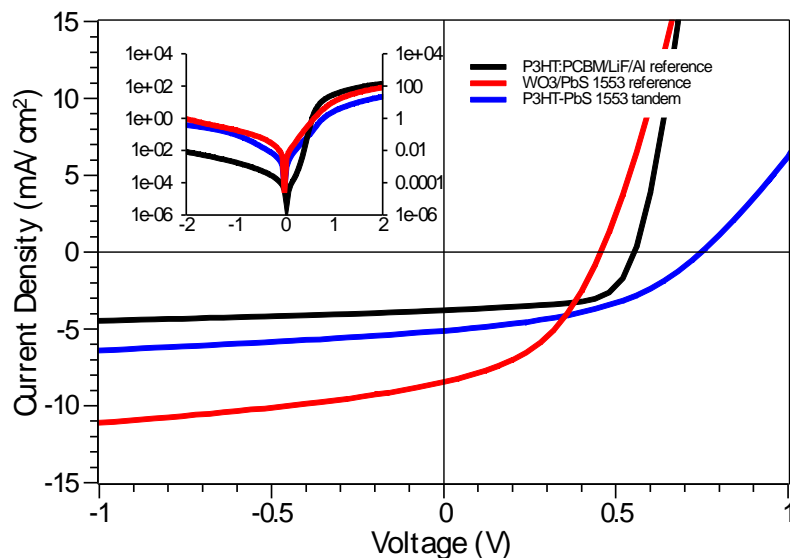


Figure 5.18: J-V curves of the ITO/PEDOT/P3HT:PCBM/ZnO/WO<sub>3</sub>/PbS/LiF/Al tandem cell and the reference cells. The thicknesses of the ZnO and WO<sub>3</sub> layer are 20 and 30 nm. The structure of the polymer reference cell is ITO/PEDOT/P3HT:PCBM/LiF/Al and that of the nanocrystal reference is ITO/WO<sub>3</sub>/PbS/LiF/Al.

Device	$V_{oc}$ (V)	$J_{sc}$ (mA/cm <sup>2</sup> )	FF	PCE (%)
P3HT:PCBM reference	0.552	3.6	0.63	1.26
PbS reference	0.455	8.3	0.43	1.65
P3HT – PbS tandem	0.747	5.1	0.43	1.64

Table 5.7: J-V characteristics of the devices displayed in Figure 5.18.

Figure 5.18 also tells us that there are still issues with the resistances in the tandem cell and in the lead sulfide reference cell. The latter suffers from a low shunt resistance, just as the previous PbS reference cell. Both cells were made on a layer of WO<sub>3</sub>, and it is likely that this layer is causing the problems, for example by changing the morphology of the lead sulfide layers. Experiments with a different interlayer anode are described later in this section. The tandem cell also has a low shunt resistance, combined with a high series resistance. This series resistance might find its origin in the thick tungsten oxide layer, and therefore additional experiments on this tandem structure were carried out where the size of the tungsten oxide layer was varied. For one tandem 15 nanometers of tungsten oxide was used and the active layers were adjusted according to new optical simulations. Another tandem was made with 45 nm of WO<sub>3</sub>. Both were damaged in the process and the power conversion efficiency did only exceed one percent for one area of the latter cell (see Table 5.8). This table also lists the parameters for a tandem cell with the exact same structure as the one in Figure 5.18 to test its reproducibility. Additionally, a P3TI:PC<sub>70</sub>BM equivalent of this structure was made. These devices did not perform well and the reproducibility of the tandem was not proven.

Device	$V_{oc}$ (V)	$J_{sc}$ (mA/cm <sup>2</sup> )	FF	PCE (%)
45 nm WO <sub>3</sub>	0.737	5.0	0.34	1.25
P3HT tandem #2	0.625	3.6	0.33	0.75
P3TI tandem	0.759	1.0	0.53	0.39

Table 5.8: J-V characteristics of polymer – PbS tandem solar cells. The first two tandems have the structure ITO/PEDOT/P3HT:PCBM/ZnO/WO<sub>3</sub>/PbS/LiF/Al. For the third tandem, the polymer blend is changed to P3TI:PC<sub>70</sub>BM. The first tandem has a 45 nm WO<sub>3</sub> layer and the second tandem is a copy of the tandem in Figure 5.18.

The intensity of the light incident on the tandem solar cell was discussed above. The fact that the mismatch factor of the tandem cell cannot be calculated brings an uncertainty to the J-V curves. Therefore, it is good to have an idea of the performance of the lead sulfide cell under reduced light intensity, to make sure that the current density in the back subcell does not deviate drastically from the value obtained from a single reference cell. For this purpose, a light intensity measurement of an ITO/WO<sub>3</sub>/PbS/LiF/Al cell was carried out. The highest light intensity used in the experiment was 100 mW/cm<sup>2</sup> and this intensity was reduced by placing neutral density filters in front of the solar cell. A summary of the light intensity dependence of the device parameters is given in Figure 5.19.

Light intensity dependence PbS 1553

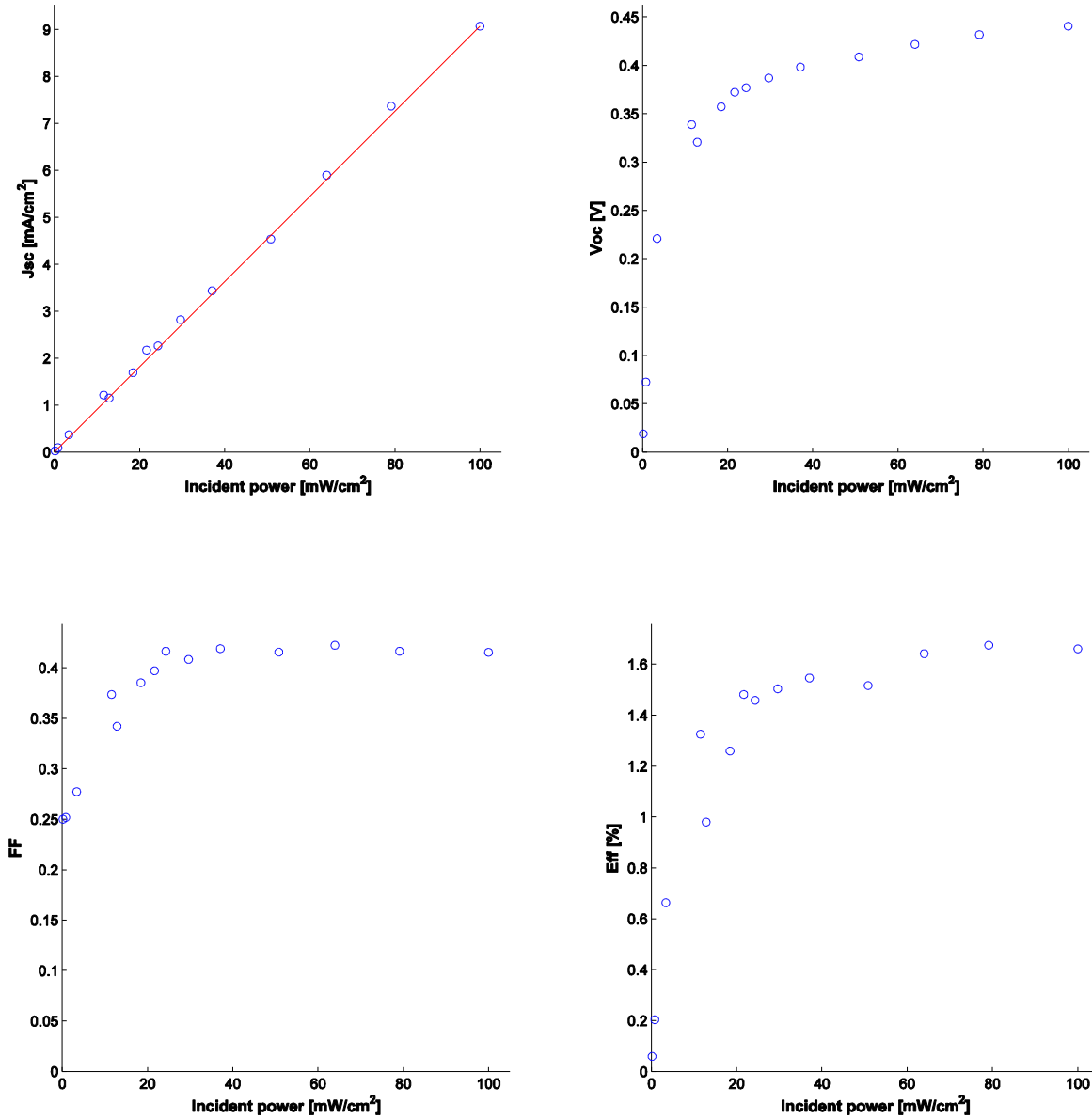


Figure 5.19: The light intensity dependence of the short-circuit current density, open-circuit voltage, fill factor and power conversion efficiency of an ITO/WO<sub>3</sub>/PbS/LiF/Al solar cell.

From these plots it is clear that the  $J_{sc}$  and  $V_{oc}$  follow the theoretically predicted dependence on the intensity, which are mentioned in the experimental chapter. The  $J_{sc}$  is more sensitive to a change in light intensities at high intensities and therefore this curve is plotted separately in Figure 5.20. Table 5.7 tells us that the actual device reached a  $J_{sc}$  of 8.3 mA/cm<sup>2</sup>, which is in agreement with the  $J_{sc}$  of 9.1 mA/cm<sup>2</sup> in Figure 5.20.

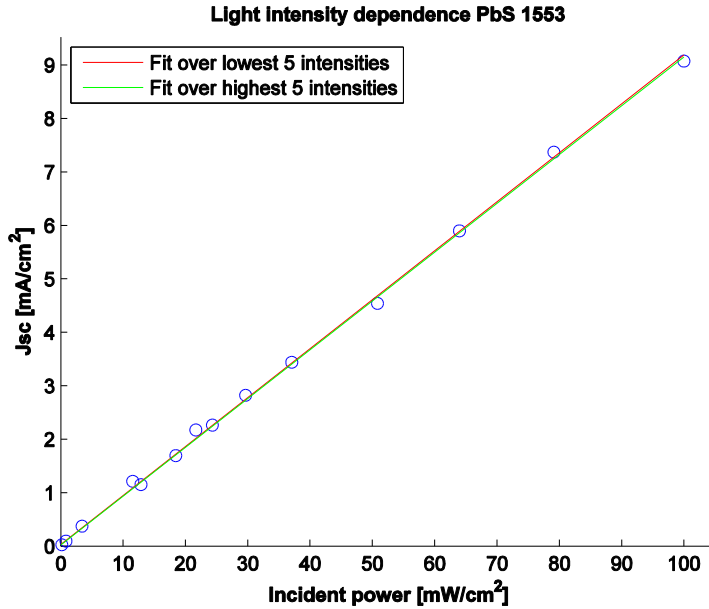


Figure 5.20: The dependence of the short-circuit current density of the PbS reference cell on the intensity of the incident light. The circles indicate the measurement points. The red and green lines are the fits of the data over the lowest five and the highest five measured intensities, respectively. As can be seen in the plot both fits are almost identical and therefore the light intensity dependence is linear over the range from 0 to 100 mW/cm<sup>2</sup>.

The intensity of the light that reaches the PbS back subcell in the P3HT:PCBM/ZnO/WO<sub>3</sub>/PbS tandem cell can be estimated using the transmittance of the P3HT:PCBM/ZnO reference cell. The transmittance was measured from 300 to 1200 nm and can be seen in Figure 5.21a. The solar spectrum (AM1.5 level) is plotted in Figure 5.21b. The intensity of the solar spectrum after being transmitted through the P3HT cell was calculated and is displayed in the same plot. The ratio of the intensity of the transmitted and incident light was found to be 0.48 over the wavelength range mentioned above. In the following, it is assumed that the entire solar spectrum is attenuated with this ratio, keeping the spectral distribution identical. This means that the intensity of the light incident on the PbS subcell is 48 mW/cm<sup>2</sup>. Looking at Figure 5.20, this would result in a  $J_{sc}$  of 4.4 mA/cm<sup>2</sup>. This current density is lower than that of the P3HT – PbS tandem solar cell and this is the result of overestimating the absorption of the P3HT subcell. In reality the light intensity at the PbS layer will be higher than that calculated from the graph in Figure 5.21b. However, this experiment gives an approximation of the current density in the back subcell and it is likely that the  $J_{sc}$  for the tandem cell is the maximum attainable value.

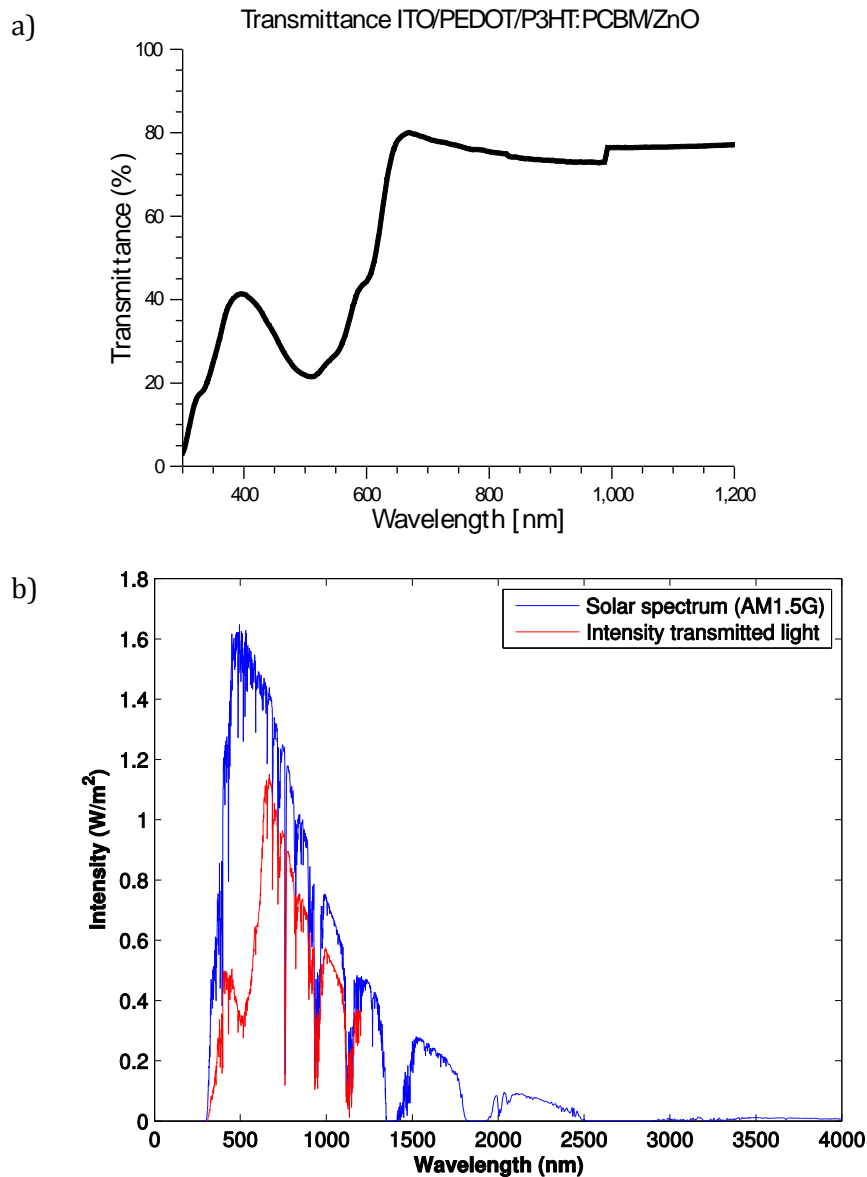


Figure 5.21: (a) Transmittance of the ITO/PEDOT/P3HT:PCBM/ZnO subcell and (b) the intensity of the solar spectrum after passing through this cell.

Despite the relatively high value for the  $J_{sc}$  of the tandem cell, the open-circuit voltage and fill factor are still low due to the damage done to the cell. After repeated failure to protect the underlying layers, it was assumed that the tungsten oxide layer was causing the problems and this layer was investigated using an atomic force microscope (AFM). Figure 5.22 makes it clear that the interlayer is not void-free. Big holes, with areas on the order of  $10 \mu\text{m}^2$  and depth of several nanometers are visible in the film. Holes of this size can easily lead to pathways for the chloroform to penetrate to the front subcell. It means that the deposition of tungsten oxide during evaporation is not uniform enough for our purpose and it should not be used as thin interlayer. It is possible that a thicker layer will lead to a non-permeable interlayer, but this is not ideal for the series resistance.

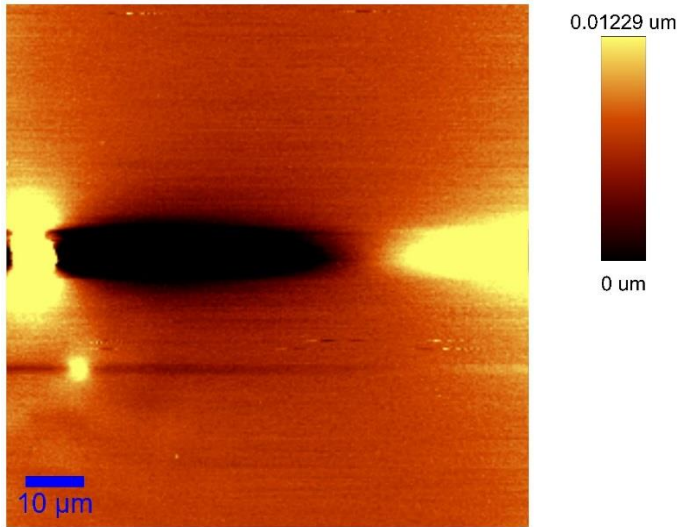


Figure 5.22: Atomic force microscopy height image of a tungsten oxide layer deposited on top of ITO/PEDOT/P3HT:PCBM. The color bar on the right indicates the height scale in the image.

There was one other material available that could serve as an anode in the device structure under investigation: molybdenum oxide. This metal oxide has a work function of -5.3 eV, as opposed to the -4.8 eV work function of  $\text{WO}_3$ . Looking at the HOMO level of the lead sulfide nanocrystals (-5.2 eV), this is not the ideal alignment of energy levels. Nevertheless, the difference is small and charge separation is still possible, though the efficiency of the charge separation will be affected. This might lead to a build-up of charge around the interlayer, resulting in a reduced current density. However, this would be a minor source of loss if the use of  $\text{MoO}_3$  in the interlayer leads to an intact tandem cell.

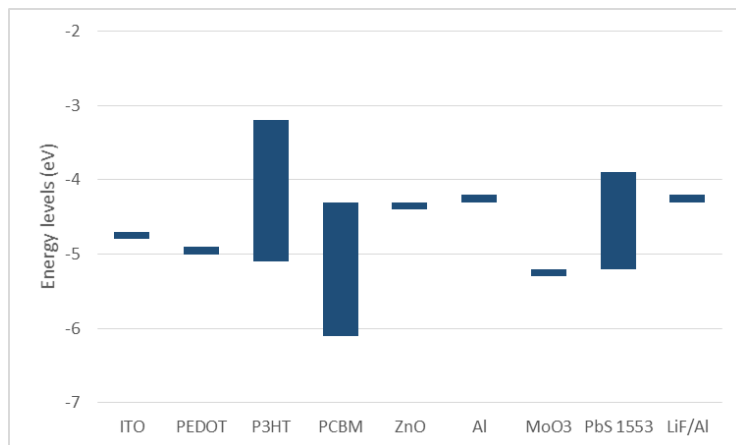
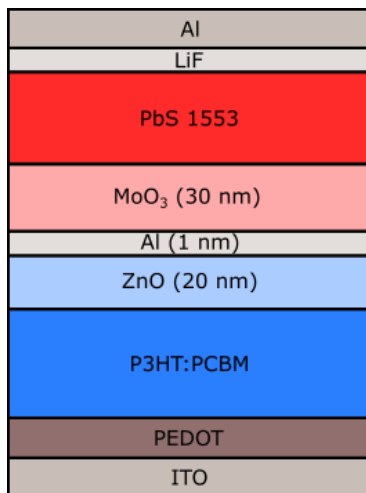


Figure 5.23: The device structure of the P3HT - PbS tandem with  $\text{MoO}_3$  as the interlayer anode. Depicted on the right are the energy levels of the tandem's materials.

To test the new anode material, a P3HT – PbS tandem was made with the structure depicted in Figure 5.23. Zinc oxide and aluminum were used as the cathode of the interlayer. The aluminum layer was inserted as an additional protective layer. Optimal thicknesses for the active layers were determined through optical modelling. According to the model, a  $J_{sc}$  of 7-8 mA/cm<sup>2</sup> could be attained when the P3HT:PCBM layer is 120 nm thick combined with a thickness of 90 nm for the nanocrystal layer. Six layers of PbS were spincoated to achieve this latter thickness.

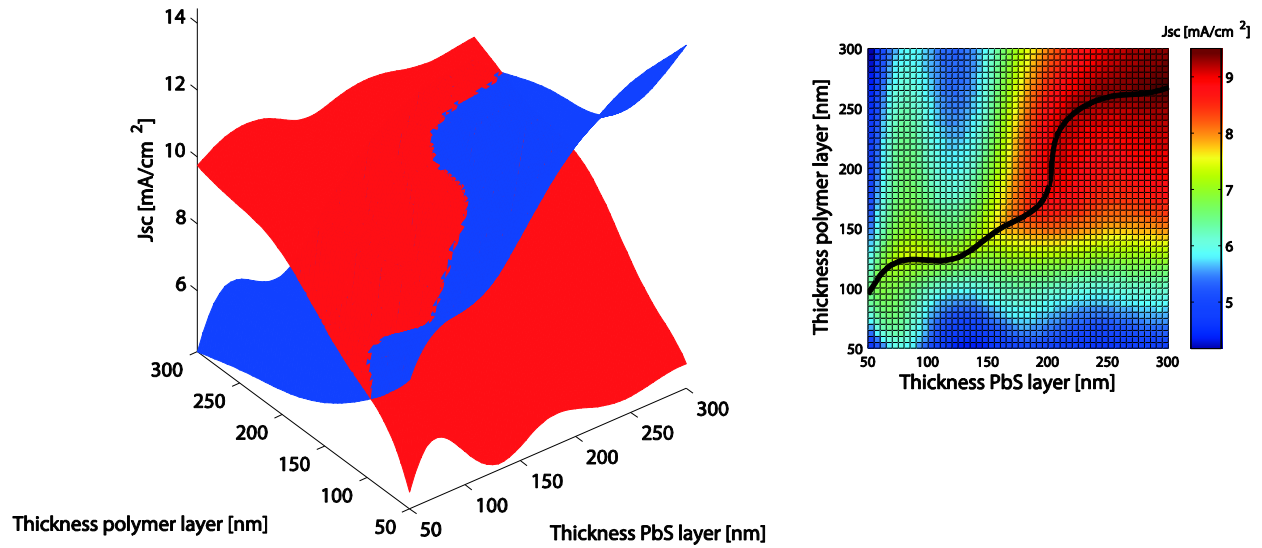


Figure 5.24: Optical simulations for the optimal thicknesses of the active layer in the structure ITO/PEDOT/P3HT:PCBM/ZnO/Al/MoO<sub>3</sub>/PbS/LiF/Al.

The deposition of the nanocrystals resulted in a slightly damaged cell, where mainly the center of the device was affected. The area where the PbS solution is deposited before the spincoating starts was discolored, indicating that some material had been removed. However, the damage was less severe than for previous cells; the outer regions of the substrate were unaffected. The device was tested and the resulting J-V curve is shown in Figure 5.25, along with that of the P3HT:PCBM reference cell (see Table 5.9 for device parameters).

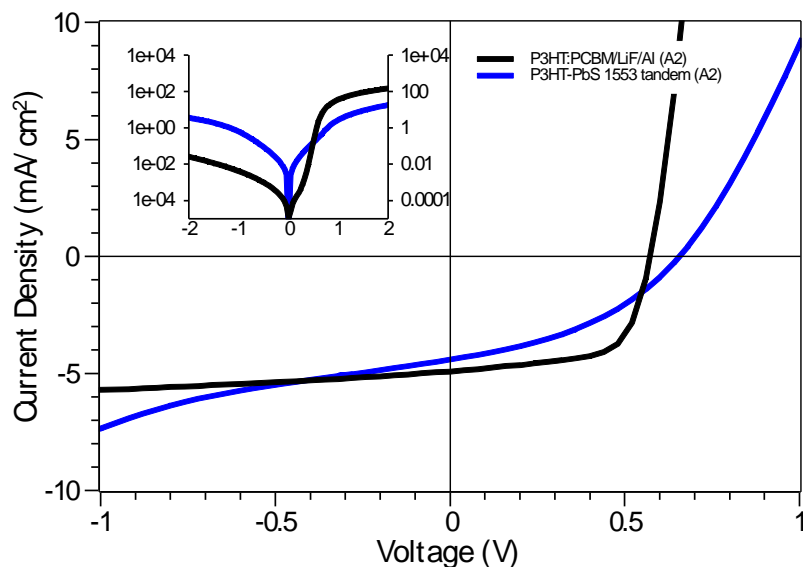


Figure 5.25: J-V curves of the tandem depicted in Figure 5.23 and the polymer reference cell.

Device	$V_{oc}$ (V)	$J_{sc}$ (mA/cm <sup>2</sup> )	FF	PCE (%)
P3HT:PCBM reference	0.571	4.9	0.64	1.79
P3HT – PbS MoO <sub>3</sub> tandem	0.656	4.4	0.39	1.14

Table 5.9: Solar cell parameters of the P3HT:PCBM/ZnO/Al/MoO<sub>3</sub>/PbS tandem and the P3HT:PCBM reference cell.

The power conversion efficiency of the tandem exceeds 1% and the  $V_{oc}$  is higher than that of the subcells. Moreover, the  $J_{sc}$  is almost equal to that of the polymer subcell. The major limiting factor for the efficiency is the low fill factor. From the J-V curve it is clear that this low fill factor is caused by a high series resistance and a low shunt resistance. The high series resistance can be explained by a build-up of charge around the interlayer due to the mismatch in energy levels. An explanation for the low shunt resistance is the damage done to the active layer, which introduces defects in the material. It is clear that this structure is not ideal for an efficient tandem solar cell. However, this interlayer offered the best protection for the front subcell during PbS spincoating. Future research on incorporating molybdenum oxide into the interlayer of polymer – lead sulfide tandem solar cells might result in high efficiencies when a suitable cathode material is available. This material should enhance the protection of the front subcell. In addition, the energy levels of the interlayer materials should be modified to match the PbS energy levels, for example by inserting additional layers.

## Chapter 6 Conclusions

The work done for this thesis focused on making a series-connected tandem solar cell with a polymer-fullerene blend as the active layer in the front cell, combined with a lead sulfide nanocrystal-based back subcell. Several solution-processed tandem cells were made for this purpose. Variations in the device structure were made by changing the polymer-fullerene blend, the lead sulfide batch and the interlayer materials. The polymer-fullerene blends that were used were P3HT:PCBM, PCPDTBT:PCBM and P3TI:PC<sub>70</sub>BM. These polymers differ in band gaps and consequently have distinct absorption spectra. The tandem structure requires good complementarity in the absorption spectra of the active layer materials as well as a delicate balance in the generation of photocurrent in each subcell. In addition to this, the energy levels of the interlayer materials have to be matched to the HOMO-LUMO levels of the front and back subcell. These requirements make the design and fabrication of tandem solar cells a complex process. The model that was used in this thesis for the optical simulations assisted in the optimization of the device structures. The simulated optimal thicknesses were used as the guidelines during the device fabrication.

The majority of the tandem cells were made with tungsten oxide as the anode of the interlayer. This material meets two out of three requirements for an ideal interlayer material. It is optically transparent (for optimal light transmission to the back subcell) and its work function is located in a good position with respect to the HOMO level of the lead sulfide nanocrystals. This enables the photogenerated holes in the back subcell to travel to the interlayer where they can recombine with the electrons from the front subcell. However, it was discovered that the tungsten oxide layer does not meet the third requirement for interlayers: it does not protect the underlying layers during the device processing. An experiment on this material was carried out where the surface morphology was investigated by atomic force microscopy. This revealed that the tungsten oxide layer was not continuous, as indicated by micrometer sized holes. Holes in the interlayer create a pathway for the solution of the back subcell to flow to the front subcell, where it dissolves the active layer materials. The damage that this does to the solar cell usually renders the device useless. Most of the tandem cells made for this thesis were damaged to such extent that the power conversion efficiencies did not exceed 1%. This means that using only the individual subcells would result in a higher value for the PCE. However, in a few cases where the tandem was damaged the device performance was better than expected.

The best tandem device was made with a structure of ITO/PEDOT/P3HT:PCBM/ZnO/WO<sub>3</sub>/PbS/LiF/Al, where the interlayer consisted of 20 nanometers of zinc oxide and 30 nanometers of tungsten oxide. Optical simulations predicted that this structure would be capable of delivering a short-circuit current density of 7 or 8 mA/cm<sup>2</sup>. The actual device had a  $J_{sc}$  of 5.1 mA/cm<sup>2</sup>, combined with an open-circuit voltage of 0.747 volt and a fill factor of 0.43. This led to a power conversion efficiency of 1.64%, which was higher than the PCE of the polymer reference cell and equal to that of the lead sulfide reference device. The  $V_{oc}$  equaled 74% of the sum of the open-circuit voltages of the subcells. Light intensity dependence measurements indicated that the device's current density was the maximum attainable value for this configuration. The photovoltaic performance could be improved by an increase in the fill factor. This parameter was low because the device suffered from a low shunt resistance. Apart from the damage that was done to the solar cell, this could be caused by the lead sulfide subcell. It was discovered that using tungsten oxide in combination with lead sulfide significantly changes the J-V curve of the lead sulfide Schottky cell. A possible explanation for this behavior is that the morphology of the nanocrystal layer is altered by the underlying

tungsten oxide layer. Attempts to reproduce these J-V characteristics with a second tandem did not give satisfactory results.

The fact that the tungsten oxide layer was causing problems led to the replacement of this layer. The only other available material suitable for hole extraction was molybdenum oxide. An interlayer of zinc oxide (20 nm), aluminum (1 nm) and molybdenum oxide (30 nm) was used in a P3HT:PCBM – PbS tandem. From optical simulations it was determined that a short-circuit current density of 7 mA/cm<sup>2</sup> was attainable. Although the device was damaged during its fabrication, it reached a PCE of 1.14%. The values for the  $V_{oc}$ ,  $J_{sc}$  and fill factor were 0.656 V, 4.4 mA/cm<sup>2</sup> and 0.39, respectively. Despite the fact that the new interlayer could not fully protect the underlying layers effectively, the damage to the cell was only limited. This means that molybdenum oxide is better for the protection of the underlying layers. However, the efficiency of the device was reduced due to a mismatch in the energy levels of molybdenum oxide and lead sulfide.

Future research should focus on finding anode materials with suitable work functions that can be inserted between the MoO<sub>3</sub> layer and the lead sulfide layer to enhance the charge transport. Another possibility is to experiment with the evaporation process for tungsten oxide in order to deposit a hole-free layer. The quality of the evaporated layer is dependent on the rate of evaporation and it is possible that evaporating with a lower rate will result in a more uniform film. The advantage of experimenting with this material is that the energy level alignment is better than that of MoO<sub>3</sub>. Finally, it is an option to find another anode material and test whether it is suitable as an interlayer material. Two candidates for interlayer anode materials are gold and vanadium oxide (V<sub>2</sub>O<sub>5</sub>). Both have a work function that matches with the HOMO level of the lead sulfide nanocrystals and they have been used in solar cell research before. However, using these materials will also lead to challenges. For example, the use of gold will have to be restricted to a thin layer since it does not have a high transmittance. Further research is needed to investigate the feasibility of making a polymer – lead sulfide tandem cell with these materials. When the current challenges are overcome, a tandem cell with a  $V_{oc}$  of 1 V and a  $J_{sc}$  of 7-8 mA/cm<sup>2</sup> can be expected. Combining this with a fill factor of at least 0.5, this could result in tandems with efficiencies of 3.5% and higher. Replacing the P3HT:PCBM blend with a more efficient alternative, such as P3TI:PC<sub>70</sub>BM, could enhance the PCE even more. This could result in a 5% tandem cell with an open-circuit voltage of 1.2 V, a short-circuit current density of 7 mA/cm<sup>2</sup> and a fill factor of 0.6.

## Bibliography

- [1] M. A. Green, K. Emery, Y. Hishikawa, W. Warta and E. D. Dunlop, "Solar cell efficiency tables (version 45)," *Prog. Photovolt: Res. Appl.*, vol. 23, pp. 1-9, 2015.
- [2] D. Zhitomirsky, O. Voznyy, L. Levina, S. Hoogland, K. W. Kemp, A. H. Ip, S. M. Thon and E. H. Sargent, "Engineering colloidal quantum dot solids within and beyond the mobility-invariant regime," *Nat. Commun.*, vol. 5, no. 3803, pp. 1-7, 2014.
- [3] M. Yuan, O. Voznyy, D. Zhitomirsky, P. Kanjanaboos and E. H. Sargent, "Synergistic Doping of Fullerene Electron Transport Layer and Colloidal Quantum Dot Solids Enhances Solar Cell Performance," *Adv.Mater.*, vol. 27, pp. 917-921, 2015.
- [4] Z. He, C. Zhong, S. Su, M. Xu, H. Wu and Y. Cao, "Enhanced power-conversion efficiency in polymer solar cells using an inverted device structure," *Nature Photon.*, vol. 6, pp. 591-595, 2012.
- [5] J. You, L. Dou, K. Yoshimura, T. Kato, K. Ohya, T. Moriarty, K. Emery, C. Chen, J. Gao, G. Li and Y. Yang, "A polymer tandem solar cell with 10.6% power conversion efficiency," *Nat. Commun.*, vol. 4, no. 1446, pp. 1-10, 2013.
- [6] M. J. Speirs, B. Groeneveld, L. Protesescu, C. Piliago, M. V. Kovalenko and M. A. Loi, "Hybrid inorganic-organic tandem solar cells for broad absorption of the solar spectrum," *Phys. Chem. Chem. Phys.*, vol. 16, pp. 7672-7676, 2014.
- [7] D. V. Talapin, J.-S. Lee, M. V. Kovalenko and E. V. Shevchenko, "Prospects of Colloidal Nanocrystals for Electronic and Optoelectronic Applications," *Chem. Rev.*, vol. 110, pp. 389-458, 2010.
- [8] X. Huang, I. H. El-Sayed, W. Qian and M. A. El-Sayed, "Cancer Cell Imaging and Photothermal Therapy in the Near-Infrared Region by Using Gold Nanorods," *J. Am. Chem. Soc.*, vol. 128, pp. 2115-2120, 2006.
- [9] V. Klimov, *Semiconductor and Metal Nanocrystals*, New York: Marcel Dekker, Inc., 2004.
- [10] S. A. McDonald, G. Konstantatos, S. Zhang, P. W. Cyr, E. J. D. Klem, L. Levina and E. H. Sargent, "Solution-processed PbS quantum dot infrared photodetectors and photovoltaics," *Nat. Mater.*, vol. 4, no. 2, pp. 138-142, 2005.
- [11] L. Brus, "Chemical approaches to semiconductor nanocrystals," *J. Phy. Chem. Solids*, vol. 59, no. 4, pp. 459-465, 1998.
- [12] A. L. Efros and M. Rosen, "The electronic structure of semiconductor nanocrystals," *Annu. Rev.*

- Mater. Sci.*, vol. 30, pp. 475-521, 2000.
- [13] K. Szendrei, Charge extraction from colloidal organic nanocrystals. PhD thesis, University of Groningen, 2011.
- [14] K. Szendrei, W. Gomulya, M. Yarema, W. Heiss and M. A. Loi, "PbS nanocrystal solar cells with high efficiency and fill factor," *Appl. Phys. Lett.*, vol. 97, pp. 203501 - 203501-3, 2010.
- [15] K. P. C. Vollhardt and N. E. Schore, *Organic Chemistry: Structure and Function* (5th ed.), New York: Freeman, 2007.
- [16] J. Nelson, "Organic photovoltaic films," *Curr. Opin. Solid State Mater. Sci.*, vol. 6, pp. 87-95, 2002.
- [17] J.-F. Chang, B. Sun, D. W. Breiby, M. M. Nielsen, T. I. Sölling, M. Giles, I. McCulloch and H. Sirringhaus, "Enhanced Mobility of Poly(3-hexylthiophene) Transistors by Spin-Coating from High-Boiling-Point Solvents," *Chem. Mater.*, vol. 16, no. 23, p. 4772-4776, 2004.
- [18] C. Kittel, *Introduction to solid state physics* (8th ed.), Hoboken: Wiley, 2005.
- [19] C. Uhrich, D. Wynands, S. Olthof, M. K. Riede, K. Leo, S. Sonntag, B. Maennig and M. Pfeiffer, "Origin of open circuit voltage in planar and bulk heterojunction organic thin-film photovoltaics depending on doped transport layers," *J. Appl. Phys.*, vol. 104, pp. 043107-1 - 043107-6, 2008.
- [20] W. Queisser and H. J. Shockley, "Detailed balance limit of efficiency of p-n junction solar cells," *J. Appl. Phys.*, vol. 32, pp. 510-519, 1961.
- [21] A. Marti and G. L. Araújo, "Limiting efficiencies for photovoltaic energy conversion in multigap systems," *Sol. Energ. Mat. Sol. Cells*, vol. 43, pp. 203-222, 1996.
- [22] R. Vogel, P. Hoyer and H. Weller, "Quantum-Sized PbS, CdS, Ag<sub>2</sub>S, Sb<sub>2</sub>S<sub>3</sub>, and Bi<sub>2</sub>S<sub>3</sub> Particles as Sensitizers for Various Nanoporous Wide-Bandgap Semiconductors," *J. Phys. Chem.*, vol. 98, pp. 3183-3188, 1994.
- [23] C. Piliago, L. Protesescu, S. Z. Bisri, M. V. Kovalenko and M. A. Loi, "5.2% efficient PbS nanocrystal Schottky solar cells," *Energy Environ. Sci.*, vol. 6, pp. 3054-3059, 2013.
- [24] N. Zhao, T. P. Osedach, L.-Y. Chang, S. M. Geyer, D. Wanger, M. T. Binda, A. C. Arango, M. G. Bawendi and V. Bulovic, "Colloidal PbS Quantum Dot Solar Cells with High Fill Factor," *ACS Nano*, vol. 4, no. 7, pp. 3743-3752, 2010.
- [25] Y. Zhou, M. Eckab and M. Krüger, "Bulk-heterojunction hybrid solar cells based on colloidal nanocrystals and conjugated polymers," *Energy Environ. Sci.*, vol. 3, pp. 1851-1864, 2010.

- [26] R. J. Ellingson, M. C. Beard, J. C. Johnson, P. Yu, O. I. Micic, A. J. Nozik, A. Shabaev and A. L. Efros, "Highly efficient multiple exciton generation in colloidal PbSe and PbS quantum dots," *Nano Lett.*, vol. 5, pp. 865-871, 2005.
- [27] W. Yoon, J. E. Boercker, M. P. Lumb, D. Placencia, E. E. Foos and J. G. Tischler, "Enhanced Open-Circuit Voltage of PbS Nanocrystal Quantum Dot Solar Cells," *Sci. Rep.*, vol. 3, no. 2225, 2013, DOI:10.1038/srep02225.
- [28] M. J. Speirs, D. M. Balazs, H.-H. Fang, L.-H. Lai, L. Protesescu, M. V. Kovalenko and M. A. Loi, "Origin of the increased open circuit voltage in PbS-CdS core-shell quantum dot solar cells," *J. Mater. Chem. A*, vol. 3, pp. 1450-1457, 2015.
- [29] M. Scharber and N. Sariciftci, "Efficiency of bulk-heterojunction organic solar cells," *Prog. Polym. Sci.*, vol. 38, pp. 1929-1940, 2013.
- [30] D.E. Carlson and C.R. Wronski, "Amorphous silicon solar cell," *Appl. Phys. Lett.*, vol. 28, pp. 671-673, 1976.
- [31] C. Piliago and M. A. Loi, "Charge transfer state in highly efficient polymer-fullerene bulk heterojunction," *J. Mater. Chem.*, vol. 22, pp. 4141-4150, 2012.
- [32] C. Goh, S. R. Scully and M. D. McGehee, "Effects of molecular interface modification in hybrid organic-inorganic photovoltaic cells," *J. Appl. Phys.*, vol. 101, pp. 114503 - 114503-12, 2007.
- [33] C. M. Proctor, M. Kuik and T.-Q. Nguyen, "Charge carrier recombination in organic solar cells," *Prog. Polym. Sci.*, vol. 38, pp. 1941-1960, 2013.
- [34] H. Hoppe and N. S. Sariciftci, "Organic solar cells: An overview," *J. Mater. Res.*, vol. 19, no. 7, pp. 1924-1945, 2004.
- [35] J. Y. Kim, K. Lee, N. E. Coates, D. Moses, T.-q. Nguyen, M. Dante and A. J. Heeger, "Efficient Tandem Polymer Solar Cells Fabricated by All-Solution Processing," *Science*, vol. 317, pp. 222-226, 2007.
- [36] A. Hadipour, B. De Boer, J. Wildeman, F. B. Kooistra, J. C. Hummelen, M. G. R. Turbiez, M. M. Wienk, R. A. J. Janssen and P. W. M. Blom, "Solution-processed organic tandem solar cells," *Adv. Funct. Mater.*, vol. 16, pp. 1897-1903, 2006.
- [37] L. A. A. Pettersson, L. S. Roman and O. Inganäs, "Modeling photocurrent action spectra of photovoltaic devices based on organic thin films," *J. Appl. Phys.*, vol. 86, no. 1, pp. 487-496, 1999.
- [38] J. Gilot, I. Barbu, M. M. Wienk and R. A. J. Janssen, "The use of ZnO as optical spacer in polymer solar cells: Theoretical and experimental study," *Appl. Phys. Lett.*, vol. 91, pp. 113520-1 -

113520-3, 2007.

- [39] L. Dou, J. You, J. Yang, C.-C. Chen, Y. He, S. Murase, T. Moriarty, K. Emery, G. Li and Y. Yang, "Tandem polymer solar cells featuring a spectrally matched low-bandgap polymer," *Nature Photon.*, vol. 6, no. 3, pp. 180-185, 2012.
- [40] T. Ameri, G. Dennler, C. Lungenschmied and C. J. Brabec, "Organic tandem solar cells: A review," *Energy Environ. Sci.*, vol. 2, p. 347–363, 2009.
- [41] X. Wang, G. I. Koleilat, J. Tang, H. Liu, I. J. Kramer, R. Debnath, L. Brzozowski, D. A. R. Barkhouse, L. Levina, S. Hoogland and E. H. Sargent, "Tandem colloidal quantum dot solar cells employing a graded recombination layer," *Nature Photon.*, vol. 5, no. 8, pp. 480-484, 2011.
- [42] M. Jørgensen, K. Norrman and F. C. Krebs, "Stability/degradation of polymer solar cells," *Solar Energy Materials and Solar Cells*, vol. 92, p. 686–714, 2008.
- [43] J. Kim, S. Kim, H.-H. Lee, K. Lee, W. Ma, X. Gong and A. Heeger, "New Architecture for High-Efficiency Polymer Photovoltaic Cells Using Solution-Based Titanium Oxide as an Optical Spacer," *Adv. Mater.*, vol. 18, pp. 572-576, 2006.
- [44] M. T. Dang, G. Wantz, H. Bejbouji, M. Urien, O. J. Dautel, L. Vignau and L. Hirsch, "Polymeric solar cells based on P3HT:PCBM: Role of the casting solvent," *Sol. Energ. Mat. Sol. Cells*, vol. 95, no. 12, pp. 3408-3418, 2011.
- [45] J. Peet, J. Y. Kim, N. E. Coates, W. L. Ma, D. Moses, A. J. Heeger and G. C. Bazan, "Efficiency enhancement in low-bandgap polymer solar cells by processing with alkane dithiols," *Nat. Mater.*, vol. 6, pp. 497 - 500, 2007.
- [46] E. Wang, Z. Ma, Z. Zhang, K. Vandewal, P. Henriksson, O. Inganäs, F. Zhang and M. R. Andersson, "An Easily Accessible Isoindigo-Based Polymer for High-Performance Polymer Solar Cells," *J. Am. Chem. Soc.*, vol. 133, pp. 14244-14247, 2011.
- [47] Z. Ma, W. Sun, S. Himmelberger, K. Vandewal, Z. Tang, J. Bergqvist, A. Salleo, J. W. Andreasen, O. Inganäs, M. R. Andersson, C. Müller, F. Zhang and E. Wang, "Structure–property relationships of oligothiophene–isoindigo polymers for efficient bulk-heterojunction solar cells," *Energy Environ. Sci.*, vol. 7, no. 1, pp. 361-369, 2014.
- [48] G. Li, R. Zhu and Y. Yang, "Polymer solar cells," *Nature Photon.*, vol. g, pp. 153-161, 2012.
- [49] Y. He and Y. Li, "Fullerene derivative acceptors for high performance polymer solar cells," *Phys. Chem. Chem. Phys.*, vol. 13, p. 1970–1983, 2011.
- [50] F. Zhang, Z. Zhuo, J. Zhang, X. Wang, X. Xu, Z. Wang, Y. Xin, J. Wang, J. Wang, W. Tang, Z. Xu and Y. Wang, "Influence of PC60BM or PC70BM as electron acceptor on the performance of

- polymer solar cells," *Sol. Energ. Mat. Sol. Cells*, vol. 97, pp. 71-77, 2012.
- [51] M. Speirs, Prospects of PbS NCs in hybrid solar cells and the effects of ligand exchange on NC properties. Master Thesis, University of Groningen, 2012.
- [52] L. Cademartiri, E. Montanari, G. Calestani, A. Migliori, A. Guagliardi and G. A. Ozin, "Size-Dependent Extinction Coefficients of PbS Quantum Dots," *J. Am. Chem. Soc.*, vol. 128, pp. 10337-10346, 2006.
- [53] S. Z. Bisri, E. Degoli, N. Spallanzani, G. Krishnan, B. J. Kooi, C. Ghica, M. Yarema, W. Heiss, O. Pulci, S. Ossicini and M. A. Loi, "Determination of the Electronic Energy Levels of Colloidal Nanocrystals using Field-Effect Transistors and Ab Initio Calculations," *Adv. Mater.*, vol. 26, p. 5639-5645, 2014.
- [54] H. B. Michaelson, "The work function of the elements and its periodicity," *J. Appl. Phys.*, vol. 48, no. 11, pp. 4729-4733, 1977.
- [55] M. Y. Chan, C. S. Lee, S. L. Lai, M. K. Fung, F. L. Wong, H. Y. Sun, K. M. Lau and S. T. Lee, "Efficient organic photovoltaic devices using a combination of exciton blocking layer and anodic buffer layer," *J. Appl. Phys.*, vol. 100, pp. 094506-1 - 094506-4, 2006.
- [56] V. Shrotriya, G. Li, Y. Yao, C.-W. Chu and Y. Yang, "Transition metal oxides as the buffer layer for polymer photovoltaic cells," *Appl. Phys. Lett.*, vol. 88, pp. 073508-1 - 073508-3, 2006.
- [57] A. K. K. Kyaw, D. H. Wang, D. Wynands, J. Zhang, T. Q. Nguyen, G. C. Bazan and A. J. Heeger, "Improved light harvesting and improved efficiency by insertion of an optical spacer (ZnO) in solution-processed small-molecule solar cells," *Nano Lett.*, vol. 13, p. 3796-3801, 2013.
- [58] H. P. Kim, A. R. b. M. Yusoff, H. M. Kim, H. J. Lee, G. J. Seo and J. Jang, "Inverted organic photovoltaic device with a new electron transport layer," *Nanoscale Res. Lett.*, vol. 9:150, pp. 1-9, 2014.
- [59] S. Chen, J. R. Manders, S.-W. Tsang and F. So, "Metal oxides for interface engineering in polymer solar cells," *J. Mater. Chem.*, 2012,22, 24202, vol. 22, pp. 24202-24212, 2012.
- [60] H. Kim and C. M. Gilmore, "Electrical, optical, and structural properties of indium-tin-oxide thin films for organic light-emitting devices," *J. Appl. Phys.*, vol. 86, no. 11, pp. 6451-6461, 1999.
- [61] B. F. Bory, P. R. F. Rocha, R. A. J. Janssen, H. L. Gomes, D. M. D. Leeuw and S. C. J. Meskers, "Lithium fluoride injection layers can form quasi-Ohmic contacts for both holes and electrons," *Appl. Phys. Lett.*, vol. 105, pp. 123302-1 - 123302-4, 2014.
- [62] J. Gilot, M. M. Wienk and R. A. J. Janssen, "Measuring the External Quantum Efficiency of Two-Terminal Polymer Tandem Solar Cells," *Adv. Funct. Mater.*, vol. 20, p. 3904-3911, 2010.

- [63] L. J. A. Koster, V. D. Mihailetschi, H. Xie and P. W. M. Blom, "Origin of the light intensity dependence of the short-circuit current of polymer/fullerene solar cells," *Appl. Phys. Lett.*, vol. 87, pp. 203502-1 - 203502-3, 2005.
- [64] L. J. A. Koster, V. D. Mihailetschi, R. Ramaker and P. W. M. Blom, "Light intensity dependence of open-circuit voltage of polymer:fullerene solar cells," *Appl. Phys. Lett.*, vol. 86, pp. 123509-1 - 123509-3, 2005.
- [65] I. Riedel, J. Parisi, V. Dyakonov, L. Lutsen, D. Vanderzande and J. C. Hummelen, "Effect of Temperature and Illumination on the Electrical Characteristics of Polymer-Fullerene Bulk-Heterojunction Solar Cells," *Adv. Funct. Mater.*, vol. 14, no. 1, pp. 38-44, 2004.

